Titanium Substitution Effects on Structure, Activity, and Stability of Nanoscale Ruthenium Oxide Oxygen Evolution Electrocatalysts: Experimental and Computational Study

Jose Fernando Godínez-Salomón,^{1,‡} Francisco Ospina-Acevedo,^{2,‡} Luis A. Albiter,³ Kathleen O. Bailey,¹ Zachary G. Naymik,¹ Rubén Mendoza-Cruz,⁴ Perla B. Balbuena,^{2*} and Christopher P. Rhodes^{1,3*}

- ¹ Department of Chemistry and Biochemistry, Texas State University, San Marcos, TX 78666, United States
- ² Department of Chemical Engineering, Texas A&M University, College Station, TX 77843, United States
- ³ Materials Science, Engineering and Commercialization Program, Texas State University, San Marcos, TX 78666, United States
- ⁴ Instituto de Investigaciones en Materiales, Universidad Nacional Autónoma de México, Mexico City, 04510, Mexico KEYWORDS: Ruthenium oxide, metal substitution, electrocatalysts, oxygen evolution reaction, proton exchange membrane electrolyzers

ABSTRACT: Proton-exchange membrane water electrolyzers produce hydrogen from water and electricity and can be powered using renewable energy; however, the high overpotential, high cost, and limited supply of the oxygen evolution reaction (OER) electrocatalyst are key factors that hinder wide-scale adoption. Ruthenium oxide (RuO₂) has a lower overpotential, lower cost and higher global supply compared with iridium oxide (IrO₂), but RuO₂ is less stable than IrO₂. As an approach to improve the catalytic stability, we report the effect of titanium substitution at different concentrations within nanoscale RuO₂, Ru_{1-x}Ti_xO₂ (x=0-50 at %), on the structure, OER activity and stability using combined experiments and theory. Titanium substitution within rutile RuO₂ affects the electronic structure resulting in regions of electron accumulation and electron depletion at the surface and shifts the d-band and O2p band centers to higher binding energies. Calculations show that the effects of Ti on electronic structure are highly dependent on not only concentration but also on the specific dopant location. From electrochemical testing and analysis of the electrolyte and simulations, titanium substitution at low concentrations (12.5 and 20 at %) improves catalyst stability and lowers Ru dissolution. Experiments of OER activity agree with theory that Ti substitution results in a higher overpotential when averaging over all adsorption sites. Theoretical analysis shows that specific sites predominately act as catalytic sites for the OER, while metal dissolution occurs at different sites. Specifically, OER has the lowest barriers at penta-coordinated Ru sites, while hexa-coordinated Ru sites have the lowest energetic barriers for dissolution.

INTRODUCTION

Rather than producing hydrogen from fossil fuels, electrochemical water splitting (overall reaction: $2H_2O \rightarrow$ 2H₂ + O₂) can produce hydrogen and oxygen from water and electricity and be powered by clean, renewable sources including wind and solar energy.1 Lowering the cost of producing H₂ from water splitting is a major goal, as outlined by the U.S. Department of Energy's Hydrogen Shot goals (cost of clean H₂: \$1 per 1 kilogram in 1 decade) and can substantially contribute to decarbonizing our energy supply system and addressing zero-emission challenges.² Proton exchange membrane (PEM) electrolyzers that function under acidic conditions offer advantages of high voltage efficiencies at high current densities, high pressure operation, and fast kinetics for the cathodic hydrogen evolution reaction (HER).3, 4 In contrast to the fast HER kinetics, the anodic oxygen evolution reaction (OER, overall reaction in acid: $2H_2O \rightarrow O_2 + 4H^+ + 4e^-$) exhibits sluggish reaction kinetics that result in high overpotentials and significant efficiency losses. 3,5 Noble metal-based catalysts (Ru, Ir, Pt) have been primarily investigated for acidic OER catalysts; however, prior work supports that all known acidic OER catalysts with reasonable activity (Ru, Ir, Pt) are also unstable and dissolve under the highly oxidative potentials ($\geq 1.5~V_{RHE}$) and highly acidic environment (pH ≤ 1) of PEM electrolyzers. 1,6,7 Obtaining highly active, stable, and lower-cost OER catalysts remains a major challenge and impediment to wide scale adoption of proton-exchange membrane (PEM) electrolyzers. 1,8,9

Iridium-based catalysts (metallic Ir, IrO_x) are currently considered to exhibit the best balance of activity and stability,¹⁰ and therefore many studies including recent work by our groups^{11, 12} and other groups^{3-5, 7} have investigated iridium-based catalysts. However, iridium has high costs and an extremely limited global supply,²¹ and exploring non-Ir catalysts is of significant interest.⁹

Ruthenium in both oxide $(RuO_x)^{13,\,14}$ and metallic^{7, 14} forms has shown substantially higher acidic OER activity compared to Ir oxide (IrO_x) and metallic Ir, respectively. The lower overpotential of RuO_x compared to IrO_x can lower the required energy input and thus reduce operating costs since input electricity cost is a primary cost driver for electrolysis.⁹ Furthermore, the relative abundance of Ru is also higher than Ir in the upper continental crust.¹⁵ The higher abundance of Ru, along with other factors relative to the market, results in a significantly lower price of Ru than Ir (Ru is ~11 % the price of Ir) and Pt (Ru is ~51% the price of Pt) (see ES1, Table S1).¹⁶

Despite the higher activities, lower costs and higher global abundance of Ru compared to Ir, Ru-based catalysts have not been widely utilized in commercial PEM electrolyzers since RuO_2 and Ru catalysts show higher instability and dissolution compared to IrO_2 and $Ir.^{7,\ 17}$ Interaction of Ru with other metals and supports influences both activity and stability. Previously reported approaches to improve the stability of Ru-based OER catalysts include Au-Ru nanoparticles, $^{18,\ 19}$ Ru_xNb_{1-x}O₂, 20 RuIr oxides, 21 Pd-Ru, 22 CrRuO_x, 23 pyrochlore-type $Y_2Ru_2O_{7-d}$ and related compositions, 24 , 25 atomically dispersed Ru on PtCu metal alloys, 26 and ultrathin RuO₂ films on 3D substrates. 27

Due to its relevance, important computational efforts have been done to understand the OER mechanisms on transition metal oxides.²⁸⁻³¹ Density functional theory (DFT)-derived mechanisms proposed by Norskov et al. address the analysis based on a single active site where the adsorbate evolution mechanism (AEM) takes place.32 From this pioneering work, some important modifications have been postulated. Shao-Horn et al., for instance, proposed the presence of exposed metal atoms on the active facet to be distributed between hexa- and penta-coordinated metal sites as well as different surface oxygen positions.33 Furthermore, other authors postulated the active participation of lattice oxygen into the oxygen evolution from its recombination with an adsorbed oxygen atom through a lattice oxygen mechanism (LOM).34 The LOM is highly dependent on the facet exposed by the catalyst nanoparticle.35 Moreover, other studies have focused their efforts on elucidating pure and doped transition metal oxides performance on OER and catalyst dissolution³⁶⁻⁴¹ showing promising results from RuO2, IrO2 and TiO2 based catalysts. Prior studies have investigated Zn-,42 Mn-,43 and Mn-Fe-doped⁴⁴ RuO₂ OER catalysts. Doping of Co within RuO2 was shown from DFT calculations to alter the electron density and influence changes in the binding energies of intermediates resulting in lower activation energies.⁴⁵ Despite higher activities, the long-term durability of Codoped RuO2 under OER conditions remains unclear due to the instability of Co under these conditions. 12,46 Further, the atomic-level effects of dopants within RuO2 on the OER activity, mechanism and dissolution are still not well understood.

Titanium is a potentially useful substituent since TiO₂ is thermodynamically stable under the highly acidic (pH \leq 1) and high potentials (>1.5 V_{RHE}) required for OER. $^{1,\,47}$ Prior work has investigated Ir-Ti mixed oxides to improve stability 48 and evaluated IrTiO $_x$ as a catalyst and support. 49 So called dimensionally stable anodes (DSAs) synthesized

by coating a solution of Ru and Ti salts onto Ti metal followed by thermal decomposition have been utilized industrially for chlorine evolution⁵⁰ and explored for OER.⁵¹ A prior study reported electrodeposited Ru_{1-x}Ti_xO₂ on metallic Ti.⁵² Rather than coating Ru_{1-x}Ti_xO₂ onto Ti metal, solution-phase synthesis routes have been investigated; however, obtaining Ti substituted within the RuO₂ phase is synthetically challenging, and a number of synthetic routes result in separate RuO₂ and TiO₂ phases.^{53, 54} Synthetic routes to substitute Ti within RuO₂ have been reported;⁵⁵⁻⁵⁸ however, the OER activity and stability of Ti-substituted RuO₂ has not been previously investigated. Here, we report the effect of Ti-substituted RuO2 at different Ti concentrations on the atomic and electronic structure, oxygen evolution activity and stability using both experimental and theoretical analysis.

RESULTS AND DISCUSSION

Morphology and Elemental Composition of Synthesized $Ru_{1-x}Ti_{-x}O_{2}$. Ruthenium oxide and Ti-substituted ruthenium oxide, Ru_{1-x}Ti_{-x}O₂, with different nominal atomic concentrations of Ti (x = 0, 12.5, 20 and 50 at. %), notated as RuO_2 , $Ru_{0.87}Ti_{0.13}O_2$, $Ru_{0.80}Ti_{0.20}O_2$ and $Ru_{0.50}Ti_{0.50}O_2$ respectively (the 12.5 at % Ti material is notated as $Ru_{0.87}Ti_{0.13}O_2$ to limit the stoichiometric notation to two decimal places), were synthesized according to the steps outlined in Figure 1a. Details of the synthesis and characterization are described in the Supporting Information. The morphology and elemental composition of the synthesized Ru_{1-x}Ti_xO₂ materials were evaluated using scanning electron microscopy (SEM) (Figure 1b-e). As shown in Figure 1b, the RuO2 sample consists of nanoscalesized particles that sometimes form larger spherical aggregates. In general, the nanoscale Ru_{1-x}Ti_xO₂ materials show heterogeneous morphologies consisting of smaller roughly spherical particles and larger prismatic shaped particles (Figure 1c-e). The different particle shapes are prominently observed within the $Ru_{0.50}Ti_{0.50}O_2$ material (Figure 1e and ESI, Figure S2). From SEM images, the samples with higher Ti concentrations show larger particle sizes and a larger number of prismatic shaped particles; however, this condition does not translate into an increase in the content of Ti within the prismatic particles, as observed by energy dispersive x-ray spectroscopy (EDS). The evaluation of the Ru:Ti atomic ratio within these different particle shapes showed a higher atomic percent of Ru within the prismatic shaped particles (ESI, Figure S2). The presence of different compositions indicates different phases are formed which correlates with x-ray diffraction and scanning transmission electron microscopy analyses discussed below. The heterogeneous composition of the materials may be related to differences in the kinetics of formation of Ru-O and Ti-O bonds,59 as the condensation reactions are affected by the different electronegativities of the metals, pH, and the type of precursors used during synthesis;59, 60 however, further studies are needed to understand the effect of synthetic parameters on the condensation reaction and growth process.

Despite the observed heterogeneity, EDS micrographs (Figure 1g-i and ESI, Figure S3) show that the overall distribution of Ti and Ru within the sample is relatively

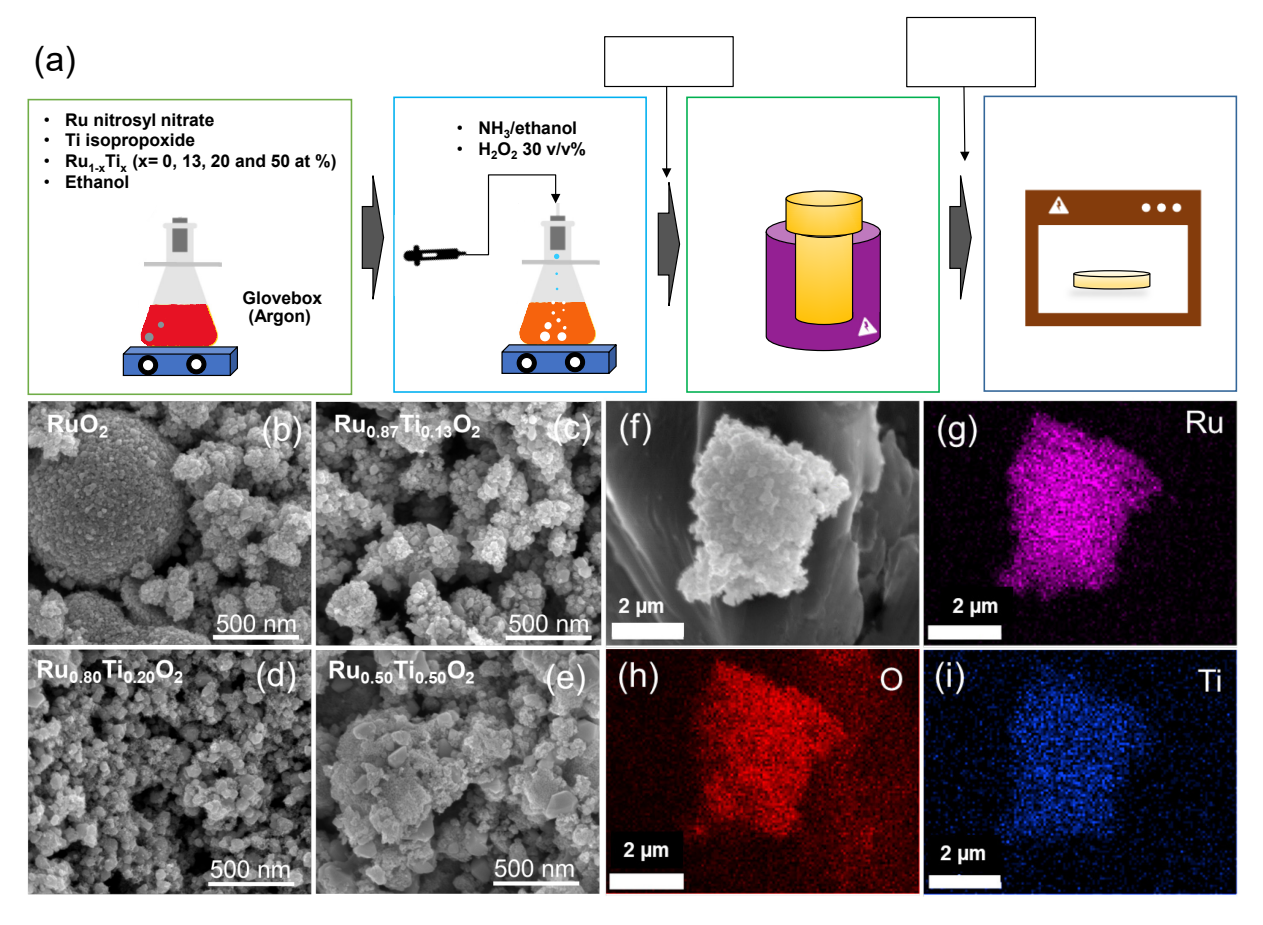


Figure 1. Steps for synthesis of $Ru_{1-x}Ti_{-x}O_2$, (x = 0, 12.5, 20 and 50 at. %), scanning electron microscopy (SEM) images of (b) RuO_2 , (c) $Ru_{0.87}Ti_{0.13}O_2$, (d) $Ru_{0.80}Ti_{0.20}O_2$ and (e) $Ru_{0.50}Ti_{0.50}O_2$; SEM image and energy-dispersive x-ray spectroscopy (EDS) mapping analysis of $Ru_{0.80}Ti_{0.20}O_2$ (f-i) showing distribution of ruthenium, titanium, and oxygen within the structure.

homogeneous at the micron scale. The Ru:Ti atomic ratios of the Ru_{1-x}Ti_{-x}O₂ samples obtained from EDS analysis are summarized in ESI, Table S2. The Ru:Ti ratios from EDS data are in the range of the nominal synthetic ratios; however, the Ru_{1-x}Ti_xO₂ materials exhibit lower experimental content of Ru compared to the synthetic ratios, which may be due, in part, to volatilization of a fraction of RuO₄61,62 during the thermal treatment step, which is in line with the observed black color of the internal walls of the muffle after thermal treatment of the material. The Ti-substituted materials show comparable BET surface areas, pore volumes pore widths, and pore-size distributions as RuO₂ (ESI, Table S2, Figure S4).

Crystalline Structure: XRD and DFT Analyses. The crystal structures of the $Ru_{1-x}Ti_xO_2$ samples were determined by powder X-ray diffraction (XRD) and Rietveld analysis. The experimental XRD patterns of $Ru_{1-x}Ti_xO_2$ and patterns for standard rutile structures of RuO_2 and TiO_2 are presented in Figure 2a. The full-scale experimental diffraction patterns, Rietveld fitting and full-scale theoretical diffraction pattern calculated from DFT-determined structures are shown in ESI, Figure S5-S7. The indexing of peaks from all samples is consistent with a tetragonal rutile phase (space group $P4_2/mnm$) as shown in Figure 2c, which agrees well with previous reports of materials synthesized under similar thermal conditions. 62,63 No phase separation corresponding to anatase or rutile TiO_2

phases was detected, which is consistent with the formation of solid solutions. Figure 2a shows the XRD region that includes the rutile (110) and (101) lattice planes. The narrower peak width of samples with Ti indicates larger crystalline domain sizes, which is consistent with the larger particles for materials with Ti observed by SEM (Figure 1). Asymmetric peak shapes were observed which suggests the presence of solid solutions with different compositions. With increasing Ti concentration, the peak associated with the (110) plane shifted toward lower $2\theta^o$ values with respect to RuO₂, while an opposite trend is observed for the (101) plane. This same behavior was obtained for the theoretical X-Ray diffraction patterns (Figure 2b).

Structural data from Rietveld fitting for the RuO₂ sample indicated the presence of a single phase with lattice parameters a=b=4.490 Å and c=3.086 Å. This structure was in good agreement with the calculated parameters determined by DFT, a=b=4.487 Å and c=3.108 Å, and those reported in literature. ⁶⁵⁻⁶⁸ The Ru_{1-x}Ti_xO₂ (x = 0, 12.5, 20 and 50 at. %) samples showed the presence of two phases of which one of them was in lower proportion of 2-14% (ESI, Table S3). In particular, the Ru_{0.87}Ti_{0.13}O₂ and Ru_{0.50}Ti_{0.50}O₂ samples showed slight asymmetry for the (110) and (101) peaks indicating structures with different Ru-Ti compositions, which was corroborated by STEM analysis (described below). The quantitative analysis of Ru_{0.87}Ti_{0.13}O₂ and Ru_{0.50}Ti_{0.50}O₂ from Rietveld fitting showed

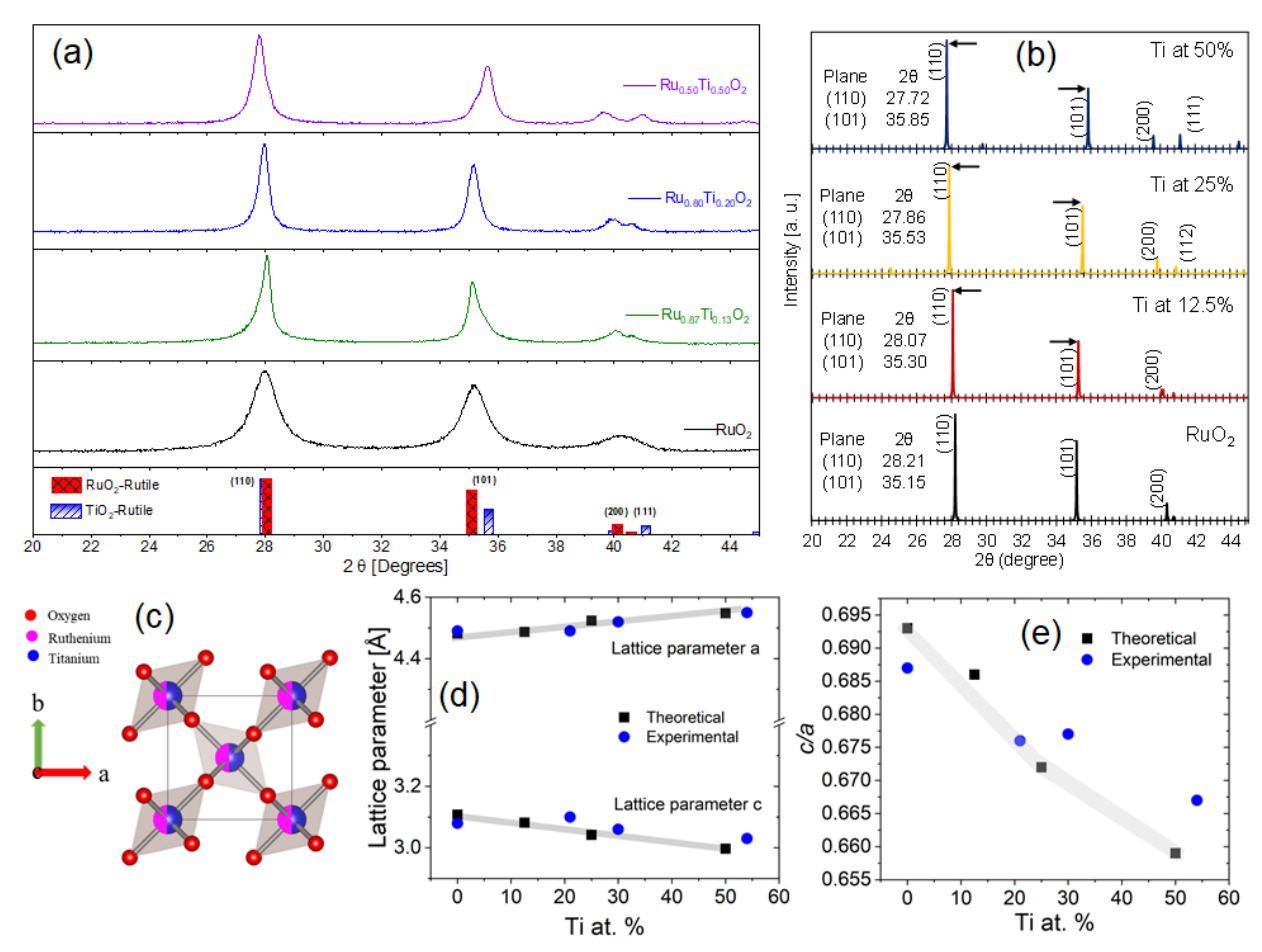


Figure 2. Experimental and theoretical crystal structures for RuO₂ and ruthenium-titanium oxides determined from XRD and from DFT calculations; (a) powder XRD patterns of RuO₂, Ru_{0.87}Ti_{0.13}O₂, Ru_{0.80}Ti_{0.20}O₂ and Ru_{0.50}Ti_{0.50}O₂ and reference patterns (RuO₂-rutile and TiO₂-rutile); (b) theoretical XRD patterns from original RuO₂ structure and Ru_{1-x}Ti_xO₂ (Ti-doped) structures at 12.5, 25, and 50% at % Ti; (c) representative crystal structure of Ru_{0.42}Ti_{0.58}O₂ found as majority phase within the sample Ru_{0.50}Ti_{0.50}O₂ showing crystallographic positions of ruthenium, titanium and oxygen within the rutile crystal structure; (d) comparison of theoretical and experimental lattice parameters (a and c) based on Ti content (at. %); experimental content of Ti corresponds to the averaged value; and (e) comparison of theoretical and experimental c/a ratios.

a total Ti concentration of 30 at. % and 52 at. %, respectively (ESI, Table S3), which differed slightly from Ti concentration determined by EDS (21 and 54 at. %), although the trend was the same. Phase separation has been reported under similar thermal treatment conditions, which is in line with the metastable behavior of $Ru_{1-x}Ti_xO_y$ materials. 69 The presence of multiple phases with different compositions increases the complexity of the analysis; however, we considered that the physicochemical and electrochemical properties would likely be dominated by the majority (86-98%) phase, and therefore we focus our analysis and discussion on the predominant phases observed.

The a and c lattice parameters from DFT and experimental analyses as a function of the composition (Figure 3d) show a lattice expansion in a and a lattice compression in c as the Ti content increases. The differing trends in the a and c lattice parameters with Ti concentration are not clearly explained on the basis of the ionic radii of Ru⁴⁺ (62.0 pm) and Ti⁴⁺ (60.5 pm) alone. Prior work supports the differing trends in the a and c

lattice parameters with Ti concentration result from the different d-electrons distribution and bonding within the rutile crystal structure.⁶³ The changes in lattice parameters with Ti concentration are also consistent with the DFT radial distribution function analysis (ESI, Figure S8) which shows that the main pair interaction distances of the Tidoped structures are shifted with respect to their values in pure RuO₂. For example, the Ru-Ru bond distance (ESI, Figure S8a) becomes shorter at high Ti concentration, while the closest Ru-Ti distance (main peaks in ESI, Figure S8b) is also shorter compared to the Ru-Ru distance in RuO2, whereas the 2nd closest remains similar to Ru-Ru in RuO₂. The original oxide exhibits two well defined Ru-O distances of 1.94 Å and 1.98 Å, and the shortest distance tends to elongate as Ti is added, with one predominant M-O distance (around 1.96 Å) found at 50% Ti concentration. Ti substitution lowers the c/a ratio as shown from experimental and DFT calculated structures (Figure 2e), and the downward trend in c/a with Ti is in line with the lower different c/a ratios of TiO₂ compared to RuO₂ from a prior study (ESI, Table S3).63 A closer look at the experimental and DFT calculated c/a ratios (Figure 3e)

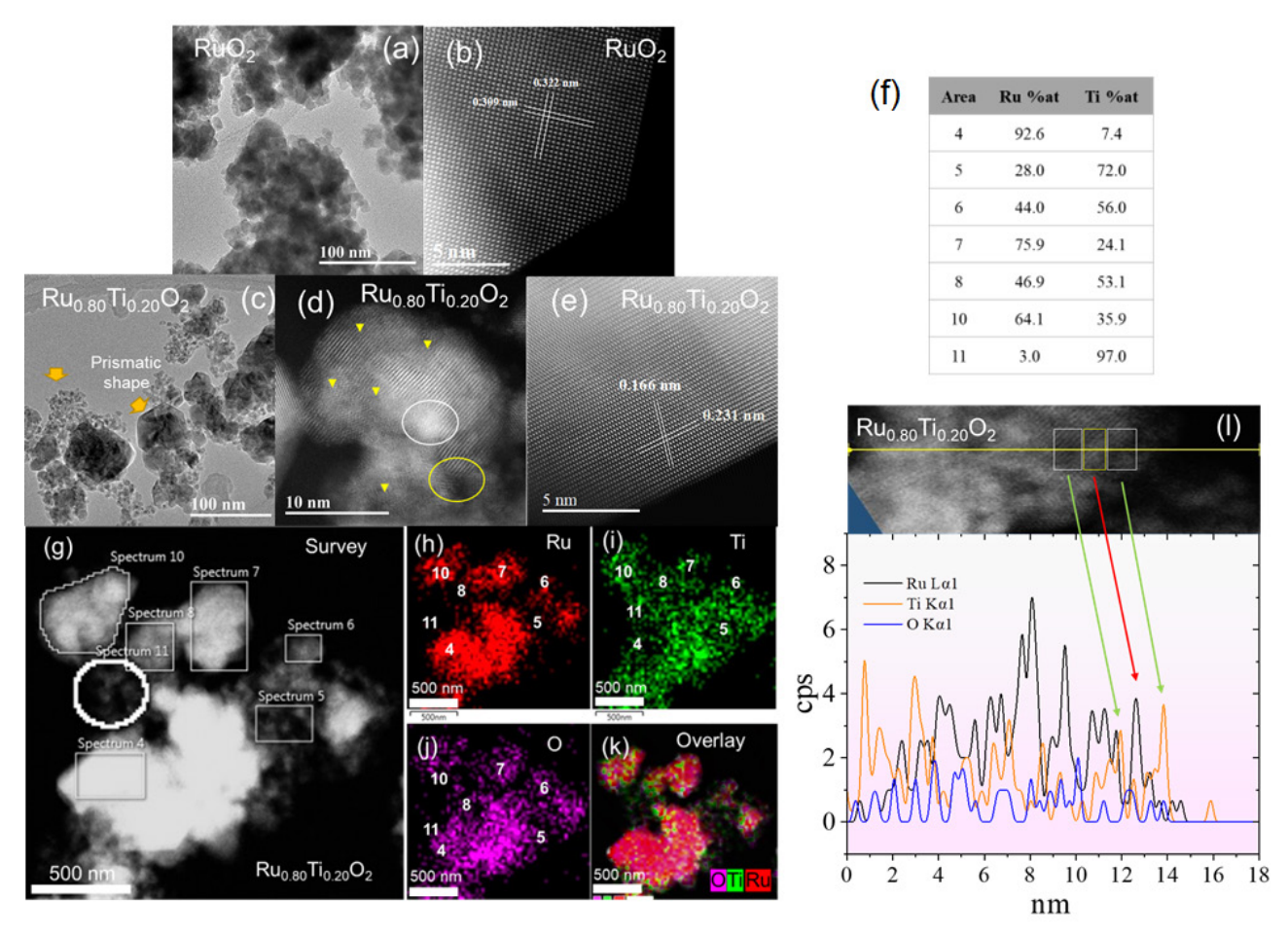


Figure 3. Low and high resolution high-angle annular dark-field scanning transmission electron microscopy (HAADF-STEM) images of RuO₂ (a-b). Low and high resolution HAADF-STEM images of Ru_{0.80}Ti_{0.20}O₂ showing particle distribution and atomic arrangement (c-e). Mapping EDS of Ru_{0.80}Ti_{0.20}O₂ over different areas (g-k), the relative Ru-Ti distribution is summarized in the table (f). Linear EDS scan and elemental profile over a cluster compose for small particles (l). Dark areas correspond to sites with high content of Ti, while bright ones, correspond to area with high content of Ru, as observed by the increasing of intensity in the profile.

showed small discrepancies which can be associated with distortions of the experimental rutile lattice, generated during the synthesis⁵⁹ and/or the heterogeneous distribution of Ti within the structure as observed by STEM discussed below.

Scanning Transmission Electron Microscopy Characterization. High-angle annular dark-field scanning transmission electron microscopy (HAADF-STEM) was performed to characterize the atomic-level structure of RuO2 and Ru_{0.80}Ti_{0.20}O2 materials. Insight into the morphology, elemental distribution, and structural organization at the atomic scale was carried out by combining HAADF-STEM mapping and linear scan EDS analyses. A representative low-resolution image of RuO2 (Figure 3a) shows small nanoscale particles with relatively narrow size-distribution and prismatic shapes. For RuO2, the analysis of the atomic structure showed a high degree of crystallinity with almost no observed defects and very sharp, clean edges (Figure 3b). The measured lattice spacing of around 0.32 nm is consistent with the (110) plane of rutile RuO₂.

Figures 3c-l show images and analysis of the Ru_{0.80}Ti_{0.20}O₂ sample. The $Ru_{0.80}Ti_{0.20}O_2$ sample containing Ti shows clusters of small nanoparticles and bigger particles with prismatic shapes (Figure 3c), consistent with the SEM analysis discussed above. Analysis at higher resolution shows small nanocrystallites within Ru_{0.80}Ti_{0.20}O₂ and corroborates the presence of short-range solid solution regions as highlighted by circles and arrows (Figure 3d). The prismatic-shaped particles within Ru_{0.80}Ti_{0.20}O₂ (Figure 3e) shows a very crystalline structure with clean edges and a homogeneous atomic distribution which suggests highly ordered sites at the surface of these particles. The EDS line scan (Figure 31) shows that Ti is atomically distributed within the structure; however, localized mapping analysis over different areas and over different types of particles (Figure 3g-k) showed heterogeneous Ru-Ti distribution. The relative Ru: Ti compositions determined from EDS from different areas is summarized in tabular form in Figure 3f. The EDS line scan (Figure 31) shows presence of Ti-rich structures on the surface of the small nanoparticles (higher intensity of Ti signal at the edges of the scan). The higher relative concentration of Ti at the surface may reduce the relative surface concentration of catalytically active Ru sites.

Computational Model. The computational methods in this study are fully explained in the Supplemental Information. Here, we provide details of the computational model and specific sites and notation used for the Ti substituents. It is a challenge to decide on a representative computational model for the surface composition of this complex system. Here, we assume that the top surface composition has the Ti concentration of the bulk system. For the surface calculations, a periodic 3-layer, 2x2 (110)-RuO₂ slab with a surface area of 6.22 x 12.68 Ų and 10 Å of vacuum space on top of the surface to avoid any periodic interactions was used. The slab's top layer is formed by eight Ru atoms (four penta- and four hexa-coordinated) and twelve oxygen (four bridge, O_B , being the most exposed oxygen atoms on the surface, and eight tri-coordinated, O_L

at the same height level as the metal atoms). For all calculations, the bottom layer, i.e., the lowest eight metal atoms and sixteen oxygen atoms are fixed, and from this slab, the top layer was doped with Ti species to achieve three different atomic concentrations: 12.5%, 25%, and 50%. Figure 4 shows the resulting surface models. The 12.5% and 25% Ti top surface coverage lead to more than one surface arrangement according to the Ti atomic configurations (Figure 4b to f). We use the nomenclature 5D and 6D to indicate the surfaces where Ti is doped on the penta- and hexa-coordinated sites respectively. To describe specific sites within each of the slabs, we used the notation Metal-Coordination_{Site} _{Number} where Metal=Ru or Ti, coordination=5 or 6, and Site Number=1-4. For example, as shown in Figure 4g, the slab with 50 at % Ti has two 5coordinated Ru sites (Ru-51 and Ru-52), two 6-coordinated Ru sites (Ru-61 and Ru-63), two 5-coordinated Ti sites (Ti-52

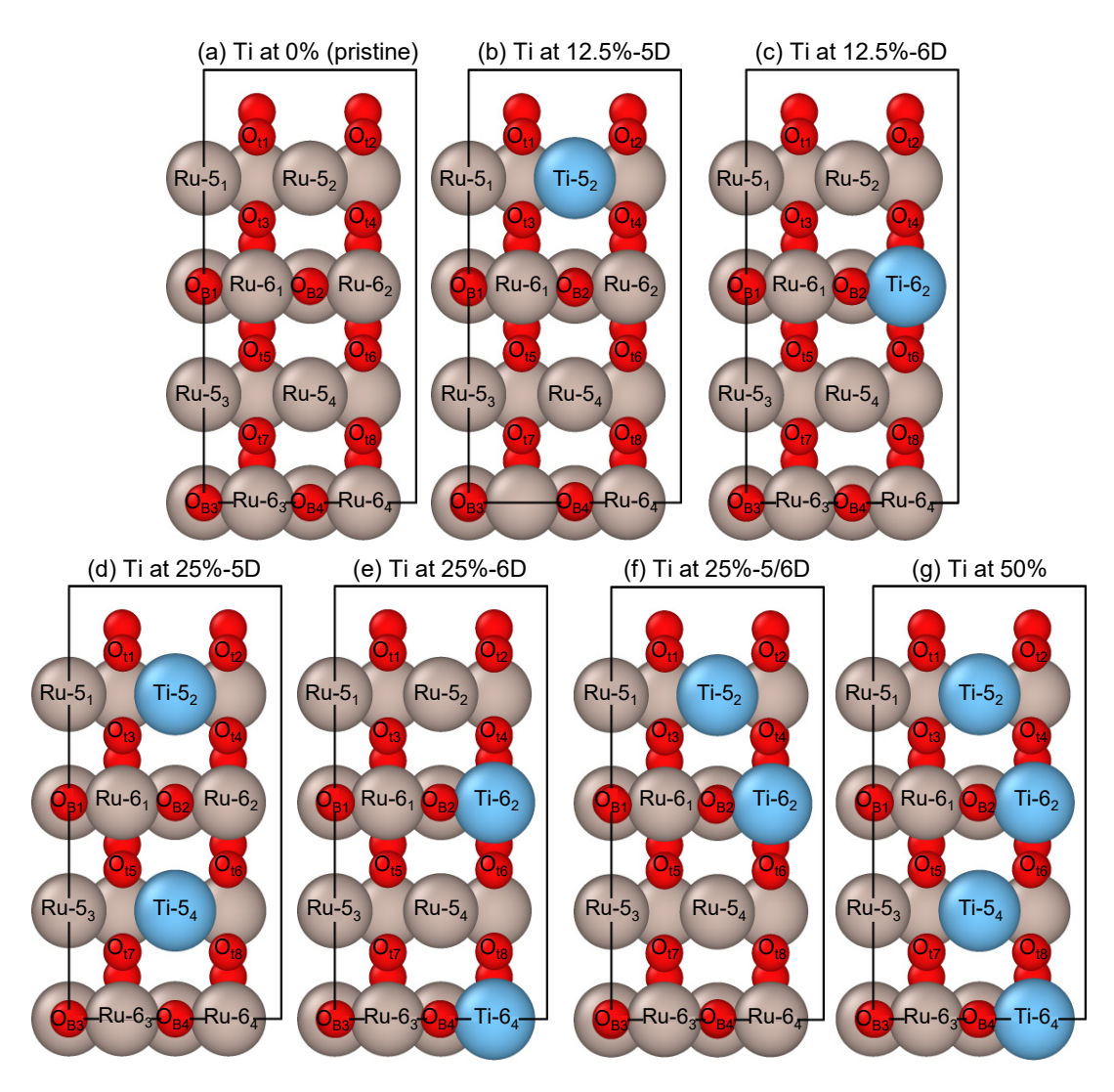


Figure 4. (a) Pristine RuO_2 surface and $Ru_{1-x}Ti_xO_2$ doped surface models for (b) 12.5% Ti-5D, (c) 12.5% Ti-6D, (d) 25% Ti-5D, (e) 25% Ti-6D, (f) 25% Ti-5/6D, and (g) 50% Ti-5/6D slabs. For each surface, starting from the top left, sites are notated as Metal-Coordination_{Site Number} where Metal=Ru or Ti, coordination=5 or 6, and Site Number=1-4. For example, Ru-54 notates a Ru atom that is 5-fold coordinated at site number 4. The site numbers from the original RuO_2 slab were maintained for the Ti-substituted slabs; oxygen atoms from O_{t1} to O_{t8} are tri-coordinated, and oxygen atoms from O_{B1} to O_{B4} are bridge- or double-coordinated. Underlined oxygen sites indicate O-Ti bonding. Color code: red, oxygen; silver, ruthenium; light blue, titanium.

and Ti-5₄), and two 6-coordinated Ti sites (Ti-6₂ and Ti-6₄). The rutile-like (110) surface is found to be the most stable facet of these crystalline compounds, including RuO2.71-73 Moreover, the stoichiometric RuO₂(110)-O_B termination is considered to be the most stable one for all (110) surfaces of crystals with the rutile structure. 74, 75 The predominance of this plane is also shown in both the experimental and theoretical findings from the x-ray diffraction and scanning transmission electron microscopy analyses, discussed above. The cyclic nature of the OER mechanism will lead to water deprotonation on undercoordinated Ru, proton adsorption on O bridge sites, as well as to variable oxygen coverage and presence of OH and water. 78, 79 work focuses on the effect of a foreign element such as Ti on the various reaction and dissolution steps, the important aspect of changes in surface composition will be included in future work.

Electronic Structure: XPS and DFT Analyses. X-ray photoelectron spectroscopy (XPS) was used to probe the effect of titanium substitution within RuO2 on the energies of core and valence electrons at the surface region (XPS survey spectra are shown in ESI, Figure S9). XPS spectra of the O2s bands of Ru_{1-x}Ti_xO₂ are shown in Figure 5a. The binding energy of the core O2s peaks of RuO2 appears at 21.4 eV, and incorporation of Ti shifts the core O2s peaks to higher binding energies (values shown in ESI, Table S7). The shifts of the O2s peak to higher binding energies for Ru₁-_xTi_xO₂ compared to within RuO₂ support that surface oxygens have gained electron density. This result agrees with the electron density accumulation observed on oxygens surrounding Ti-doped atoms, determined by DFT (Figure 5e) and is also in line with a previous study that reported a higher O2s binding energy of oxygen within rutile TiO₂ (22.4 eV) compared to within RuO₂ (21.1 eV).80 The O1s peak was also analyzed and can be deconvoluted into contributions of O-Ru, O-Ru satellite, Ti-O, and O-C components (ESI, Figure S10, Table S7),81,82 with the O-Ru satellite and Ti-O bands too close in binding energy (< 1 eV) to be adequately resolved. The relative intensity of the O1s peak corresponding to Ti-O increases with Ti concentration. as expected. Fitting analysis of the Ru3d and overlapping C1s region (ESI Figure S11, Table S7) shows Ru 3d_{5/2} and 3d_{3/2} peaks with binding energies consistent with Ru⁴⁺ within an anhydrous rutile structure.81 The fitting analysis of the overlapping region of Ti 2p_{3/2}, Ti 2p_{1/2} and Ru 3p_{3/2} peaks (ESI Figure S12, Table S7) shows a main Ti 2p_{3/2} peak with binding energy consistent with Ti4+ within the structure.82 In addition, a Ti $2p_{3/2}$ peak (relative area $\sim 5\%$) at lower binding energy is also observed. The lower binding energy Ti 2p_{3/2} peak is consistent with the binding energies reported for Ti³⁺;82 however, prior work also supports that Ti 2p peaks can be influenced by final state screening effects⁸³ and therefore further analysis is needed to confirm the origin of the lower binding energy Ti 2p peak.

XPS data of the valence bands of $Ru_{1-x}Ti_xO_2$ are shown in Figure 5b, and an expanded view near the Fermi level is shown in Figure 5c. The valence bands of RuO_2 and $Ru_{1-x}Ti_xO_2$ arise from bonds between valence electrons of O^{2-} ([He] $2s^22p^6$), Ru^{4+} ([Kr]4d⁴), and Ti^{4+} [Ar]3d⁰ and can be understood based on prior work to describe the energy level diagrams of rutile oxides.^{63, 84} In agreement with

Goodenough's model for the electronic structure of rutile oxides,84,85 the valence bands shown in Figure 5d can be described as consisting of (i) two bands with dominant 0 2p character (notated as $O2p_{\sigma}$ and $O2p_{\pi}$) and (ii) metal d-bands that lie above the O 2p bands and are at or near the Fermi level. The notation of the bands is based on the symmetry of the orbitals with respect to the axis defined by the chain of octahedra within the rutile structure,86 where each oxygen anion has three co-planar near-neighbor cations, and the anion $2p_{\pi}$ orbitals are directed perpendicular to this plane. The octahedral coordination environment of the metal sites (MO₆, M=Ru⁴⁺ or Ti⁴⁺) splits the five d orbitals into higher energy, doubly degenerate eg states and lower energy, three-fold degenerate t_{2g} states. However, the orthorhombic component of the crystalline field completely removes the degeneracies of the d-states, and the three t_{2g} orbitals split into two d_{π} orbitals and a d_{\parallel} orbital directed along the c-axis. Based on the d^4 electron configuration of Ru^{4+} , the two d_{π} orbitals are fully occupied, while the d⁰ configuration of Ti⁴⁺ has two empty d_{π} orbitals. The energy levels and occupancies of d-electrons within rutile oxides also explains how TiO_2 (d⁰) is an insulator, while RuO_2 (d⁴) exhibits metallike conductivity. ESI, Figures S13 and S14 provide all the calculated Density of States (DOS) contributions of the individual orbitals in the bulk and surface top layer respectively.

From XPS experiments, Ti substitution is observed to shift the $O2p_{\pi}$ bands to higher binding energies (Figure 5b), and similarly the Ru d_{π} peaks are shifted to slightly higher binding energies (Figure 5c); values are provided in ESI, Table S8. In addition, the intensity of the Ru d_{π} peaks relative to the O2p bands is lowered with Ti substitution (Figure 5b), which is expected since Ti substitution lowers the relative concentration of Ru at the surface. The shifts in the valence $O2p_{\pi}$ and Ru d_{π} peaks indicate that Ti substitution affects the electron density distribution around oxygen and metals within the structure. The shifts to higher binding energies of the O2p (as well as O2s and O1s) peaks with Ti substitution are in-line with different electronegativities of six-coordinated Ru⁴⁺ (χ = 1.848) compared to Ti^{4+} ($\chi = 1.730$)⁸⁷ that result in more basic Ru-O-Ti bonds compared to Ru-O-Ru bonds. The shifts of the valence Ru d_{π} peaks are related to the different c/a ratios (Figure 2c) based on the Goodenough model, which showed the relative energies of the da and da orbitals depend on the c/a ratio within the unit cell.88

DFT analyses yield further insights into the Ti-induced electronic effects. An essential characteristic of RuO_2 is its conductor or metallic behavior, manifested in the absence of band gap at the Fermi energy level, as well as a conduction band gap up to 10.4 eV.^{89, 90} Figure 5d summarizes the calculated total density of states (TDOS) relative to the Fermi level, and the results of the d- and p-band center calculations for each bulk system are presented in ESI, Table S4. Although the general conducting characteristic from RuO_2 is not altered, Ti contributes new states above the Fermi energy while reduces the states population on and below the Fermi energy. Titanium substitution results in shifting of the d-band center from -1.11 eV for RuO_2 to -1.32 eV for 50 at% Ti substituted RuO_2 , away from the Fermi level (ESI, Table S4). This effect

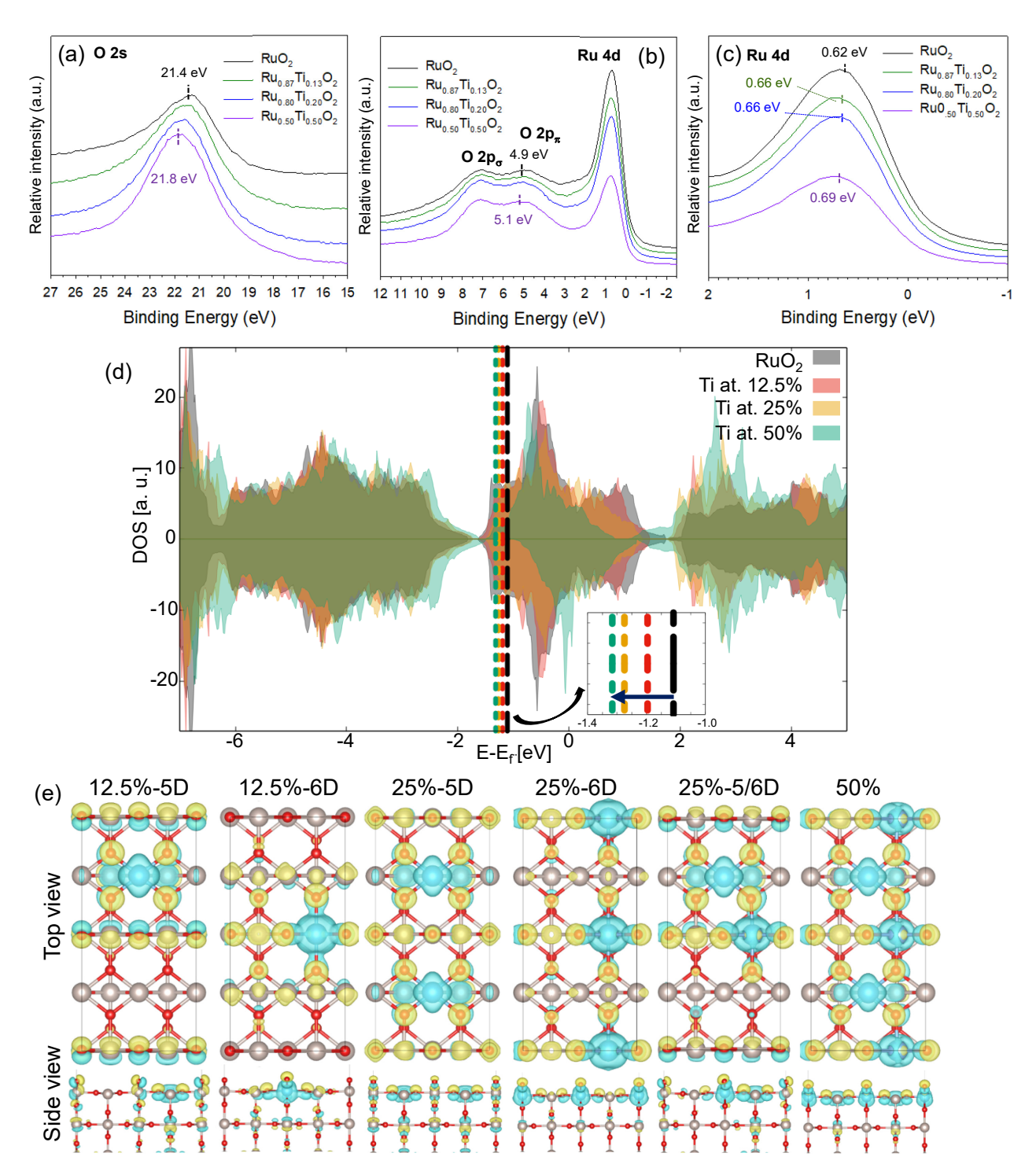


Figure 5. Experimental X-ray photoelectron spectra (XPS) of RuO₂, Ru_{0.87}Ti_{0.13}O₂, Ru_{0.80}Ti_{0.20}O₂ and Ru_{0.50}Ti_{0.50}O₂ in the (a) O 2s region, (b) valence band region, and (c) expanded view of the valence band region from -1 to 2 eV; (d) DFT calculated total density of states (TDOS) and d-band center for original RuO₂ (grey) and Ru_{1-x}Ti_xO₂ at 12.5% (red), 25% (yellow), and 50% (green) Ti concentration. Vertical dashed lines indicate the d-band center shift to lower values shown in Table 3; and (e) electron density difference $\Delta \rho = \rho_{Ru_{1-x}Ti_xO_2} - \rho_{RuO_2}$ showing electron density accumulation (yellow) and depletion (light blue) for 12.5%-5D, 12.5%-6D, 25-5D, 25-6D, 25% 5/6D, and 50% doped slabs.

may be related to the TiO_2 semiconductor nature.⁹¹ ESI, Figure S13 shows the contributions of the Ru-4d, O-2p, and Ti-3d bands to the bulk TDOS, while ESI, Figure S14 summarizes the top layer Ru-penta and hexa-coordinated

4d, O-2p, and Ti-3d bands contribution to the surface TDOS. As Ti substitutes Ru, the oxide becomes spin-polarized, especially the 4d states of the metal atoms but also the O 2p (ESI, Figure S13). The effect is even more pronounced on

the surface, inducing reactivity enhancement or depletion in specific sites (ESI, Figure S14).

The surface d-band center (ε_d) is an approximate reactivity descriptor that has been used to describe the interaction between adsorbate valence states and the s and d states of a transition-metal.92 For the (110) surface, ESI, Figure S14 identifies differences between Rupenta and hexa-coordinated 4d-band contributions to the TDOS and shows the computed values for the Ru active sites (i.e., penta-coordinated) band center. The TDOS population and the changes in the d-band center of the surface top layer resemble the bulk structure. However, the surface d-band center is a direct indicator of adsorbate-surface interaction, and, when shifted down with respect to the Fermi energy, reflects a weakening in adsorbates adsorption.93 Interestingly, ESI Figure S14 shows that the Ti effect is highly dependent not only on concentration but also on the specific dopant location. At 12.5% Ti, with Ti-6D sites the dband center is shifted much farther to the left (-1.45 eV) compared to the shift observed with Ti-5D sites (-1.40 eV). At 25% Ti, we confirm this trend as we detected a lower shift for Ti-5D sites (-1.43 eV) compared to Ti-6D sites (-1.48 eV) as shown in ESI, Figures S14d-e. For 25% Ti, an intermediate value (-1.46 eV) is observed when both dopant sites are present (for the 5/6-D slab) as shown in ESI, Figures S14f, hinting for the reduced reactivity effects from Ti-6D sites.

Similarly, the centroid of the projected density of states of the O 2p orbitals relative to the Fermi energy, or the O 2p-band center, has been used as electronic descriptor for a variety of properties in different oxides. 94, 95 ESI, Table S4 presents the O 2p-band center calculated for the bulk structures simulated in this work. In agreement with the dband behavior and with the XPS shifts in the O-binding energy, the O 2p-band center shows a trend of having more negative (away from the Fermi level) values as the Ti concentration increases (-3.05 for RuO2; -3.19 eV for 50 at% Ti substituted RuO₂). Moreover, an interesting effect is observed on the exposed (110) surface. ESI, Figure S14b,d shows that the prevalence of Ti-5D sites shifts the O_B 2pband center to more negative (away from the Fermi level) values relative to the pristine RuO2 surface, but the presence of Ti-6D sites (ESI, Figure S14c, e, f, and g) induces a shift to less negative values (closer to the Fermi level) in the same descriptor. This is in agreement with the expected O p-TM d-band hybridization due to the large overlapping between the Ti 3d and O_B 2p states,⁹⁴ and it aligns the above discussed d-band center shift.

After elucidating the effects in core electron regions, we carried out integrated projected crystal orbital Hamilton population (IpCOHP) calculations using the local orbital basis suite toward electronic-structure reconstruction (LOBSTER)⁹⁶⁻⁹⁹ software package in order to understand the effect of Ti in bonding interactions. The IpCOHP serves as an indicator of the bonding strength interaction between two specified atoms, i.e., the more negative the IpCOHP is, the stronger the atom pair interaction, and the higher the energy cost to remove any of the two species. Table S5 and Table S6 show the average value of the computed IpCOHP for different M-O pairs in the bulk and surface structures, respectively. Two trends emerge: the Ru-O pairs show a

weaker value that becomes more evident as the Ti concentration increases, and the Ti-O pairs are the weakest independently of Ti concentration. Moreover, Table S6 illustrates that the M-O_B interactions are stronger, as evidenced by more negative IpCOHP, than the M-O_t ones.

Up to this point, we demonstrated the influence of Ti presence in both RuO2 bulk and (110)-surface structures based on XPS, DFT-derived d-band and O2p band center shifts, and M-O bond strengths. Stronger binding energies of the O core electrons in the Ti-doped structures revealed by XPS were confirmed by the O2p band shifts, and by formation of weaker M-O bonds. In addition to Ti concentration, the location of the dopant was found to be an important factor. A useful way to visualize this effect is through the electronic density difference $\Delta \rho =$ $\rho_{Ru_{1-x}Ti_{x}O_{2}}-\rho_{RuO_{2}}$ as reported in Figure 5e. A significant electron depletion (light blue) is obtained at the doped sites (Ti atoms) and electron accumulation (yellow) between the doped sites and the neighbor O_B and O_t atoms. It is worth noticing how the presence of only 5D metal sites (Ti-5D) induces a slight electron depletion on the neighboring Ru penta-coordinate atoms, while having only 6D metal sites (Ti-6D) induces a small electron density accumulation on the same Ru sites. These observations agree with the relatively weaker O-Ru bonds on the Ti-doped surfaces, being slightly stronger on 6D than on 5D surfaces, concluded from Table S5. The bottom part in Figure 5e (noted "side view") shows the effect of surface Ti on the subsurface layers, beyond the second and even third layer of the slab. This subsurface effect is enhanced as the surface concentration of doped sites increases, in agreement with previously reported work in both RuO2 and IrO2-doped surfaces. 45, 100 The presence of Ti-6D or both 5D- and 6D sites highly influences the electron accumulation on the O_B atoms bonded to them, which are expected to be active sites on proton exchange reactions. Besides the bond strengths shown in ESI, Table S5 and the XPS results, the electronic effect is confirmed by the Bader electronic charges analysis¹⁰¹⁻¹⁰³ summarized in ESI, Tables S9 and S10. Compared to the pristine surface, the Bader charges on the Ru atoms of 5D surfaces at 12.5% Ti (ESI, Table S10) show subtle increases suggesting higher oxidation states for 5coordinated Ru atoms and more reduced oxidation states for 6-coordinated Ru atoms. On 6D surfaces, the 5coordinated atoms are more reduced, whereas the 6coordinated keep about the same charge as on RuO2. At higher Ti concentrations, similar charge patterns exist. Accordingly, the O atoms become less negative with respect to those in the pristine RuO₂, whereas the O on the 6D surfaces are more negative, and the trend is more evident as Ti concentration increases. The less negative charges especially on the O_B atoms may align with a trend to more covalent Ru-OB bonds, which during electrochemical oxidation may help reactions that require bond breaking or forming, whereas the more negative O values indicate more basic metal-oxygen bonds.

The Bader estimate of the atomic charges is less accurate than other methods to identify changes in the oxidation states, which is why we discuss the atomic magnetization next. As discussed briefly above, the (110)-RuO $_2$ cleaved surface is spin-polarized (ESI, Figure S14)

while the bulk structure is not (Figure 5d and ESI, Figure S13), in agreement with previous reports, ¹⁰⁴ and this spin difference becomes more noticeable with the increase in Ti concentration. Understanding the spin polarization characteristics is important as it correlates to the structure's magnetization and to changes in the oxidation states of the surface atoms. 105, 106 Previous reports suggested that this property may play a significant role in the electrolysis of water¹⁰⁴ while informing about the oxidation state and electronic distribution. We compared the magnetic moment of the metal atoms on the surface of the RuO2 and Ru_{1-x}Ti_xO₂ slabs with their average Bader charge, following the effect of Ti-D on Ru atoms, as shown in Table 1. Our calculations show that Ti atoms keep a defined closed range for both the magnetic moment and the Bader charge regardless of their concentration and coordination, with average values of 0.024 µB and 2.34 |e|, respectively. Table 1 shows the magnetization on the Ti-5D and Ti-6D sites in the 12.5% and 25% slabs, and the combination of the two types in the 25%-5/6D and 50% slabs. Posysaev et al. showed a correlation between the average Bader charge and oxidation states for binary oxides in single- and mixed-valence compounds and surfaces. 107 Based on this correlation, Ti atoms in our calculated systems show a clear +4 oxidation state in their low spin configuration. For the clean RuO2 surface atoms, Table 1 Table 1-shows a very well-defined set of values for the penta- and hexa-coordinated metal atoms. Torun et al.¹⁰⁴ reported that the stronger spin polarization effect corresponds to the 0.652 µB from the hexa-coordinated metals compared to the average -0.127 μB from the pentacoordinated sites, suggesting a possible change in the oxidation state of the respective metal atom. For the Ru atoms, the charge range in Table S5 suggests a +4 compound, but the changes in magnetization and spin difference from DOS analysis indicate a possible preferential variation between low and high spin distribution for the remaining 4d⁴ valence electrons. High spin configuration is possible when the crystal field splitting energy (Δ_0) is low relative to the spin-pairing energy (P), which are determined by the tendency for electrons to repel each other and the energy cost to pair electrons. 108 There are no studies of this nature in RuO2 systems, and more details should be addressed in future work. However, from

Table 1, we can clearly identify classes of Ru atoms. We used colors to differentiate them. In pure RuO2, there are two type of Ru atoms (characterized by their magnetic moment and Bader charge): Ru bonded to Ot atoms (pentacoordinated, colored blue) and Ru bonded to OB (hexacoordinated, colored green), with magnetic moments in agreement with those reported by Torun et al.¹⁰⁴ At 12.5% Ti, the two types of Ru atoms still display similar magnetic moment and Bader charge as in the pristine surface, except for the Ru atoms located closest to a Ti atom (Ru-51 in the 5D surface, and Ru-6₁ in the 6D surface appear to be in a higher oxidation state, colored yellow and red, respectively). In the 25% Ti surface, the 5D surface is less changed compared with RuO2, but the 6D surface follows a similar trend as the 6D at 12.5%, with the Ru atoms located close to Ti appearing in a higher oxidation state (red). When Ti is doped both in 5 and 6D at 25%, we see the same oxidation trend as in the 5D and 6D at 12.5%. Large oxidation effects are also detected on the Ru atoms close to the Ti atoms on the 50% surface, where the purple color indicates a different magnetic moment trend in the Ru 5coordinate atoms. Judging from the changes in atomic magnetic moments, these differences reflect alternative distributions of the external d-electrons in the t2g and eg orbitals due to a ligand effect, that can also be observed in the DOS shown in ESI, Figure S14. Thus, Ru atoms in the vicinity of Ti atoms may exist in a higher oxidation state that will affect the reactions on these sites. However, as discussed below, only penta-coordinated sites were found to stabilize adsorbates. We hypothesize (and come back later to this point supported by with additional simulations) that Ru-penta-coordinated atoms participate actively in the OER reaction, whereas the hexa-coordinated ones may contribute to stabilize the structure from undergoing the corrosion reaction.

Experimental Analysis of Electrochemical Oxygen Evolution Reaction Activity. The initial surface condition was evaluated from a thin-film of $Ru_{1-x}Ti_xO_2$ (0, 12.5, 20 and 50 at. %) supported on a gold electrode at a loading of 25 μg_{Cat} cm⁻², in Ar-saturated 0.1 M HClO₄, using cyclic voltammetry (CV). The CVs (ESI, Figure S15) showed very similar voltammetric features for all samples. The presence of titanium within the RuO_2 structure did not result in any observable new oxidation/reduction process in comparison

Table 1. Magnetic moment (MM) and average Bader charge |e| for surface metal atoms on RuO₂ and Ru_{1-x}Ti_xO₂ slabs. Bold, underlined numbers indicate Ti-D sites. Magnetic moments for RuO₂ surface penta-, hexa-coordinated, and O_B and O_t (not shown in Table) atoms are in agreement with previous reports from ref.⁹³ Different colors are used to group the same trends in the MM and charge values.

Slab	0%		12.5%-5D		12.5%-6D		25%-5D		25%-6D		25%-5/6D		50%	
Coord.	MM	Bader	MM	Bader	MM	Bader	MM	Bader	MM	Bader	MM	Bader	MM	Bader
Position	[μΒ]	e	[µB]	e	[μΒ]	e								
51	-0.13	1.65	0.390	1.74	-0.227	1.59	-0.302	1.72	-0.399	1.63	0.347	1.69	-0.656	1.72
52	-0.12	1.65	0.028 ^{Ti}	2.34 Ti	-0.227	1.59	0.023 Ti	2.34 Ti	-0.399	1.63	0.025 Ti	2.31 Ti	0.024 Ti	2.30 Ti
53	-0.12	1.65	-0.263	1.66	-0.227	1.59	-0.301	1.72	-0.398	1.63	-0.292	1.63	-0.656	1.72
54	-0.13	1.65	-0.155	1.67	-0.227	1.59	0.023 Ti	2.34 Ti	-0.398	1.63	-0.228	1.66	0.024 Ti	2.30 Ti
61	0.652	1.92	0.720	1.77	1.376	2.02	0.88	1.91	1.367	2.00	1.440	1.99	1.541	2.05
62	0.652	1.92	0.721	1.77	0.022 Ti	2.41 Ti	0.88	1.91	0.016 Ti	2.43 Ti	0.027 Ti	2.19 Ti	0.034 Ti	2.35 Ti
63	0.652	1.92	0.721	1.77	0.596	1.92	0.88	1.91	1.367	2.00	0.664	1.85	1.541	2.05
64	0.652	1.92	0.720	1.77	0.696	1.89	0.88	1.91	0.016 Ti	2.43 Ti	0.735	1.87	0.034 Ti	2.35 Ti

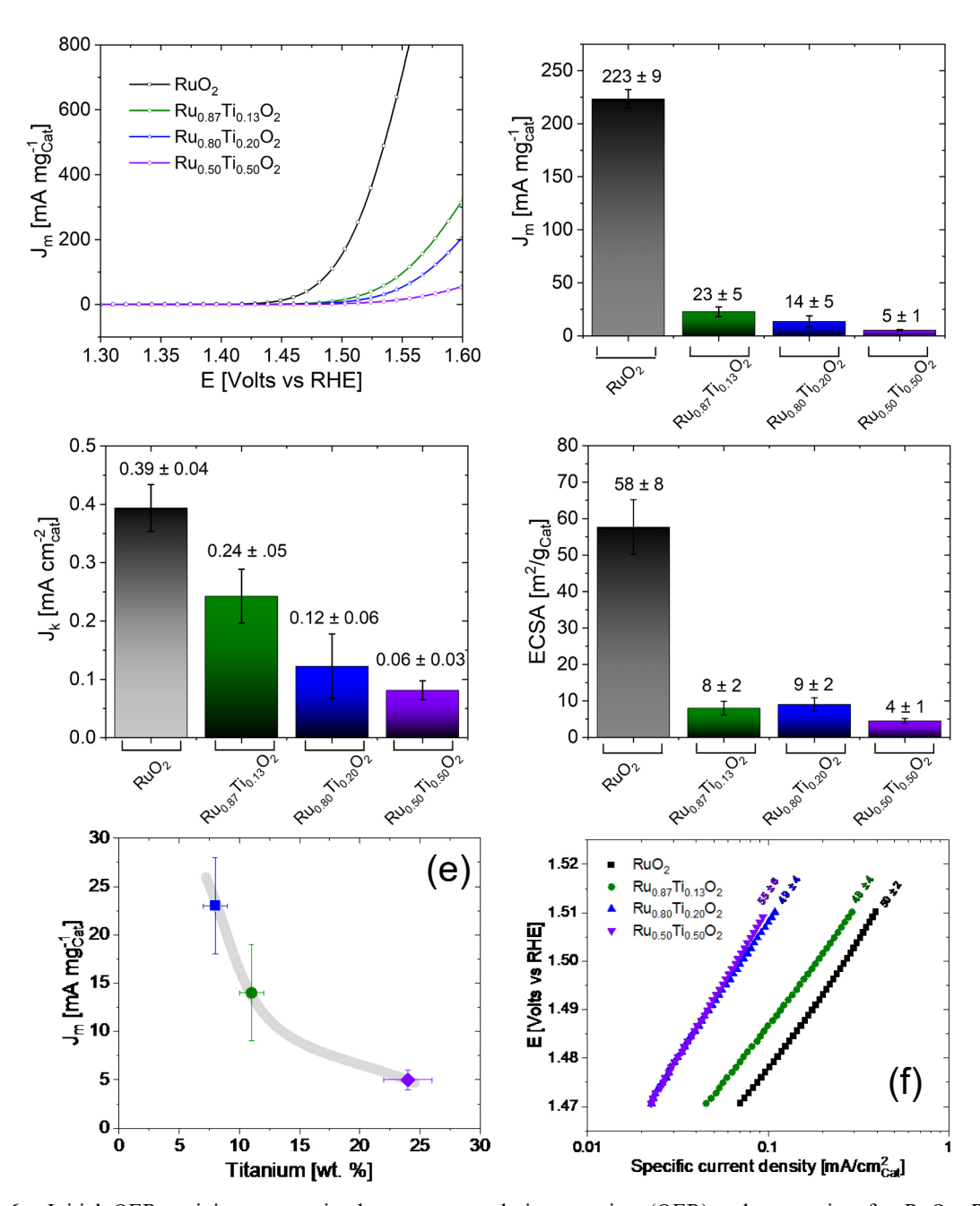


Figure 6. Initial OER activity current in the oxygen evolution reaction (OER) voltage region for RuO₂, Ru_{0.87}Ti_{0.13}O₂, Ru_{0.80}Ti_{0.20}O₂ and Ru_{0.50}Ti_{0.50}O₂ tested in Ar-purged 0.1 M HClO₄ under rotation at 2500 rpm; (a) current from linear sweep voltammetry, normalized to catalyst mass; (b) comparison of OER mass activities at 1.51 V_{RHE}; (c) comparison of OER specific activity at 1.51 V_{RHE} normalized to electrochemical surface area; (d) comparison of electrochemical surface area (ECSA) determined by double layer capacitance; . (e) Comparison of the OER mass activity with the content of Ti at.%; (f) Tafel plots and slopes of RuO₂, Ru_{0.87}Ti_{0.13}O₂, Ru_{0.80}Ti_{0.20}O₂ and Ru_{0.50}Ti_{0.50}O₂ within the 1.47-1.51 V_{RHE} voltage range determined by linear sweep voltammetry and normalized to catalyst electrochemical surface area.

to undoped RuO₂. However, a lower current is observed with increasing Ti concentration, which is consistent with lower surface area determined from BET analysis (ESI, Table S2) and larger particle sizes observed by SEM and STEM. The electrochemical active surface area (ECSA) (Figure 6d) shows similar trends when compared to the Brunauer–Emmett–Teller surface area from nitrogen physisorption; however, the surface areas obtained by the

electrochemical method were significantly lower (ESI, Figure S16). Similar behavior was reported by Faustini et al.,¹⁰⁹ suggesting that alternative approaches to determine ECSA should be further explored.

The initial OER electrocatalytic activity of the samples was assessed using the three-electrode setup, and the current was normalized by both ECSA and catalyst mass

(Figure 6a-c). Figure 6a corresponds to the current from linear scan voltammetry at a scan rate of 20 mV s⁻¹, after ohmic drop and background correction, normalized by catalyst mass. The mass and specific OER activities obtained from LSV at 1.51 V are summarized in Figure 6b and Figure 6c. The mass activity of the synthesized nanoscale RuO₂ (223 mA/mg_{cat}) was at least an order of magnitude more active than the catalysts with Ti (i.e. 23 to 5 mA/mg_{Cat}). Figure 6e shows a clear reduction of mass activity with the increase of Ti content. Both STEM (Figure 3) and XPS (ESI, Figure S9) support Ti species at the surface which reduces the number of catalytically active (i.e. RuO_x) surface sites.

The OER specific activity, related to the effectiveness of the reaction per active site, was also higher for $RuO_2 \, (0.39 \, \text{mA/cm}^2_{\text{cat}})$ in comparison to $Ru_{1\text{-x}} Ti_x O_2 \, (0.24 \, \text{to} \, 0.06 \, \text{mA/cm}^2_{\text{cat}})$; however, these differences were smaller in comparison to the differences in mass activity. The OER specific activity shows a clear decrease with increasing Ti concentration, with the specific activity trend $RuO_2 > Ru_{0.87} Ti_{0.13} O_2 > Ru_{0.80} Ti_{0.20} O_2 > Ru_{0.50} Ti_{0.50} O_2$. The direct comparison of activities among the literature is complicated by different experimental conditions and analyses used for the evaluation of oxygen evolution reaction; however, our synthesized RuO_2 shows a specific activity that is within the range of values reported for RuO_2 by other groups (ESI, Table S11).8, 13, 24, 110

The decrease in specific activity by the incorporation of titanium within the RuO2 phase can be associated to different factors. As observed from our DFT calculations. the electronic structure was significantly affected by the presence and concentration of Ti (Figure 5), and the electronic effects are highly site-dependent. Changes in the electron density distribution around Ru-active sites from Ti substitution modifies the adsorption/desorption energy of oxide/hydroxide species and influences the oxygen evolution reaction. As discussed further below using DFT analysis, we were able to determine that Ti-substituted into specific sites resulted in a higher activation energy than within the undoped structure. We also note that changes to the electronic conductivity due to Ti substitution, and/or the presence of a small (\sim 5%) amount of Ti³⁺ (from XPS analysis, ESI, Figure S12, can influence the measured OER activity. Several prior studies have reported a reduction of conductivity of Ru_{1-x}Ti_xO₂ with higher percent of Ti, affecting the activity.53, 64, 67, 111 Prior studies of Ru_{1-x}Ti_xO₂ coatings⁵¹ and electrodeposited Ru_{1-x}Ti_xO₂ (x=0.31, 0.61)⁵² on metallic Ti report higher OER activity with Ti incorporation compared to RuO2, which is different than our study of Ru_{1-x}Ti_xO₂ prepared via wet chemistry which shows lower mass and specific OER activity with Ti incorporation. The differences may be due to different synthesis methods, structural differences, specific surface sites expressed, and experimental methods and analysis used to determine OER activity.

The Tafel plots (Figure 6f) within 1.47 to 1.51 V_{RHE} (iR-corrected potentials) showed average Tafel slopes with very similar values for all catalysts (i.e., 48 to 55 mV dec⁻¹). The linear behavior in this potential region confirms a kinetically controlled process. ¹² The values of Tafel slopes are in good agreement with those commonly reported in literature for RuO_2 . ¹¹² The similarity of the slopes suggests

that similar mechanisms occur on the RuO_2 and $Ru_{1-x}Ti_xO_2$ catalysts, and at least from Tafel analysis, Ti substitution does not result in a significantly different reaction mechanism. A prior theoretical study of the OER process on RuO_2 (110) reported the Tafel slope was influenced by surface rearrangement. Tafel slope to specific theoretical reaction pathway is affected by a number of factors (e.g. symmetry factor, contribution of adsorbed species, rearrangements of reaction sites, and influence of the electrolyte, etc.) Which complicates the direct unambiguous assignment of the reaction mechanism from the experimental Tafel slope alone.

Computational Analysis of Reaction Mechanism.

To determine how Ti substitution influences the OER, we considered that after the water oxidation steps, the OER may go through three possible mechanisms, Direct Oxygen Recombination Mechanism (Mechanism 1), O and OH Recombination Mechanism (Mechanism 2), and Associative Mechanism (Mechanism 3), which are described by the following reaction steps (* represents an active site).

Water Splitting

$$2 H_2O + 2^* \rightarrow 2 OH^* + 2 H^+ + 2 e^-$$
 (1)

$$20H^* \rightarrow 20^* + 2 H^+ + 2 e^-$$
 (2)

Oxygen Evolution

Mechanism 1: Direct Oxygen Recombination Mechanism

$$0^* + 0^* \to 0_2^* \tag{3}$$

Mechanism 2: O and OH Recombination Mechanism

$$0^* + 0H^* \to 00H^*$$
 (4)

$$00H^* \rightarrow 0_2 + H^+ + e^-$$
 (5)

Mechanism 3: Associative Mechanism

$$0*+ H_2O \rightarrow 0OH^* + H^+ + e^-$$
 (6)
 $0OH^* \rightarrow 0_2 + H^+ + e^-$ (7)

All three mechanisms have the same first and second oxidation steps (Eq. 1 and Eq. 2) which we refer to as "water splitting steps". The oxygen evolution mechanisms differ in the steps to form O-O, and we refer to these steps as "oxygen evolution steps". The following sections describe the effect of Ti substitution on the reaction energies and activation energies of the water splitting and oxygen evolution steps.

Water Splitting. Relative reaction and activation energies for the first and second oxidation stages (Eq. 1 and Eq. 2) of the water molecule are shown in Figure 7a and b, and values are provided in ESI, Table S12. Adsorption was evaluated on all non-equivalent penta-coordinated sites for both Ru and Ti sites (ESI, Table S13). No favorable adsorption was found on hexa-coordinated sites. The first oxidation stage (eq. 1) has an exothermic nature (Figure 7a, and ESI, Table S12). The reaction energies (blue columns) become less exothermic at low Ti concentrations for Ti sites in all surfaces and for Ru sites on 6D surfaces. However, at higher Ti concentrations the exothermicity increases on the Ti sites. Most of the reaction coordinate profiles are barrierless or have very low activation energies ranging up to 0.09 eV.

The second water oxidation stage (eq. 2) shows a clearer dependence on the reaction site and titanium

concentration: reactions on Ru sites (Figure 7b and ESI, Table S12) have lower activation energy (orange column) compared to the pristine RuO_2 surface, with activation energies ranging up to 0.32 eV and reaction energies between -0.16 and -0.01 eV. The energy profiles are mostly like the pristine surface, and less improvement is found on the 25%-6D and 12.5%-6D surfaces, revealing that the Ti role depends on the doped site location. On the other hand, reactions on Ti sites have considerably higher activation barriers and endothermic energies, and therefore the reaction on Ti sites for this step does not have a high

probability. For all Ti-5D surfaces, activation and reaction energies are quite similar to each other, with an increase up to 66% in the activation energy compared to the pristine RuO_2 surface. Thus, for this reaction step, the actual reaction performance on Ti-D sites is independent of their concentration on the surface.

These water-splitting energetic results agree with studies done in similar systems. 45,114 The barrier-less initial oxidation stage suggests a spontaneous reaction. To confirm this, we carried out ab initio molecular dynamics

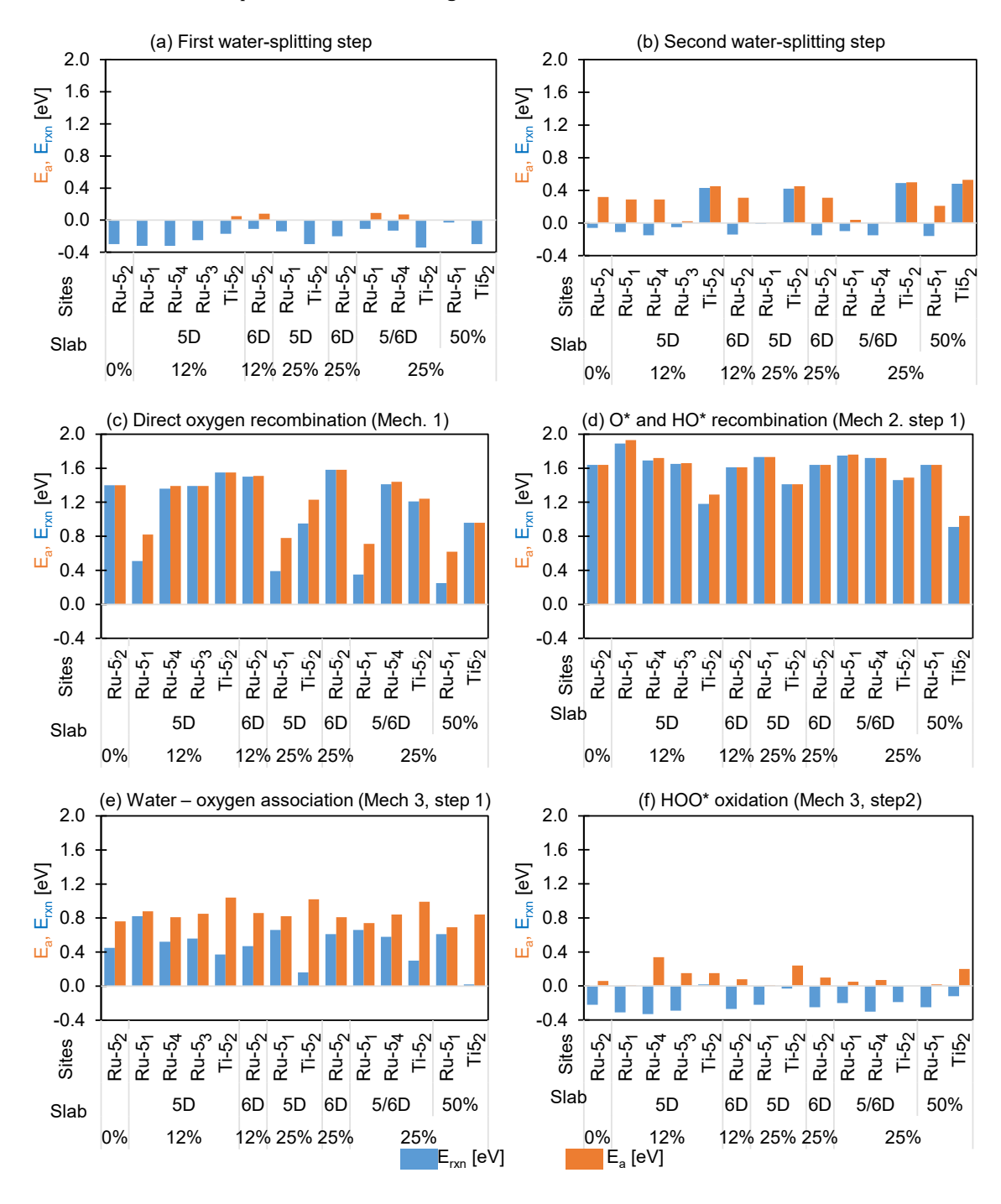


Figure 7. Relative reaction (blue) and activation energies (orange) for the (a) first and (b) second water splitting steps; (c) direct oxygen recombination mechanism; (d) first step of the oxygen and hydroxide recombination mechanism; and the (e) first and (f) second stages of the water-oxygen associative mechanism.

(AIMD) simulations up to 20 ps. ESI, Figure S18 (and supporting text in ESI) summarizes three of the study cases evaluated at 20 ps: the pristine RuO₂ surface, and the 25%-6D and 50% Ti coverage. Snapshots shown for each case (ESI, Figure S18) allows the observation of the spontaneous first oxidation reaction and an interesting dynamic proton exchange on the Ti-doped surfaces within the timeframe of the simulations. On the other hand, no second water oxidation was observed within the same simulation timeframe, as expected due to the larger barriers. The explicit solvation effect included in the AIMD simulations supports concluding that: 1) earlier water splitting is detected in the Ti-doped surfaces compared to the pristine surfaces; 2) in all cases, water splitting does not occur from the direct molecule-surface interaction but with active presence of free water molecules, and this is a frequently observed interaction; 3) the presence of Ti sites promotes a dynamic proton exchange on the surface that favors water splitting.

Oxygen Evolution Steps: a) Direct oxygen recombination. In Mechanism 1, two water molecules undergo complete oxidation (steps 1 and 2) to form two 0* species on adjacent active sites, followed by their combination on the surface to form O₂ (eq. 3). When evaluated on the pristine RuO2 surface, the reaction energy is very unfavorable (1.40 eV) being a totally uphill reaction. When Ti is added into the system, two general trends are observed; the first one is that Ti-5D sites improve the energetics of the closest 5-coordinate Ru sites reducing the endothermic reaction energies and the activation energies for the 50%, 25%-5D, 25%-5/6D, and 12.5%-5D slabs (Figure 7c). Moreover, the reaction on Ti-5D sites also shows an improvement for the 50% and 25%-5D slabs. This is interesting because even though the reaction and activation energies on Ti are considerably high, for this step, the Ti presence induces an overall better performance with respect to the pristine RuO₂ surface for this mechanism. Figure 7c shows that all other Ru sites (those not closest to the Ti-5D site) do not show any improvement. The energetics in these sites are like the original oxide sites, and the presence for Ti-6D sites, makes the reaction slightly less favorable on the remaining penta-coordinated sites. These results are explained from the adsorption energies of the atomic and molecular oxygen reported in ESI, Table S13. 0* adsorption is considerably weaker on Ti-5D than on Ru sites, with differences ranging between 0.74 and 1.11 eV compared with the Ru site that is neighboring a Ti site. Similar phenomena occur for the coupled 0^*-0^* and 0_2^* , where their adsorption energies are weaker when evaluated on Ti-5D than on Ru sites.

b) Oxygen and hydroxide recombination. Mechanism 2 (eq. 4 and 5) considers the combination of adsorbed oxygen with a partially oxidized hydroxide molecule (OH*) that forms an adsorbed hydroperoxyl group (OOH*), which undergoes subsequent oxidation to form O_2 . The first step (eq. 4), summarized in Figure 7d, is the least favorable reaction of all evaluated in this study, with a reaction energy of 1.64 eV and a totally uphill reaction for the pristine RuO_2 surface, which remains unaltered the 25%-6D and 50% cases (Figure 7d). In the 12.5%-5D, 25%-5D, and 25%-5/6D configurations, the reaction becomes even less favorable

with reaction energies up to 1.89, 1.75, and 1.73 eV, and activation energies of 1.93, 1.76, and 1.73 eV (all uphill, no transition state detected), respectively. Although 00H* adsorption on Ti-5D sites is weaker by about 0.4 eV compared to the adjacent Ru sites, reaction and activation energies for 00H* formation on Ti-5D sites are lower, with the 50% coverage being the best performance with 0.91 and 1.04 eV reaction and activation energy, respectively. The 00H* oxidation step (eq. 5) is the same as the one discussed below (eq. 7) for the associative mechanism.

c) Associative mechanism. In Mechanism 3, a free water molecule reacts with an adsorbed oxygen to form a hydroperoxyl group, which then follows the oxidation mechanism reacting with the surface oxygen to form O_2 (eq. 6 and 7. Mechanism 3). The reaction and activation energies are summarized in Figure 7e and f. The first step (Figure 7e) on the pristine RuO₂ surface is endothermic with 0.45 and 0.76 eV reaction and activation energy, respectively, becoming less endothermic on the Ti sites, and the trend increases at higher Ti concentrations. Although the reaction on Ru sites becomes more endothermic compared to the pristine surface, the activation energy decreases as the concentration of Ti increases, which is aligned with the easiness of water splitting observed in presence of Ti. The activation energy for this step is higher in all Ti sites than that on the pristine oxide surface. The second OER step (eq. 5 and 7 for Mech. 2 and 3, respectively) is exothermic and the presence of Ti improves the exothermicity of the Ru sites, with the Ru sites far from Ti showing lower activation barriers. Ti-5D sites exhibit less exothermic behavior. On the other hand, the activation energies are in the range of 10-2 to 10-1 eV, which gives an insight into the almost spontaneous nature of this step.

In summary, the DFT reaction energetics and barriers suggest that Ti effect on oxygen evolution is highly dependent on the type and location of the dopant site and on Ti concentration. The Ti-5D sites induce a better performance of the neighboring Ru-5 sites. Even though that improvement is not enough to make OER mechanisms 1 and 2 favorable, lower activation energies are found in Figure 7c and d in presence of Ti-5D sites. Overall, reactions on Ti sites are the least favorable of all, except for the first step of the oxygen and hydroxyl recombination; however, the presence of predominant 5D sites over 6D sites (as for the 50%, 25%-5/6D, and 25%-5D slabs) improves the energetics of Ru-5 sites. The 12.5%-5D slab also shows an improvement in the Ti's Ru-5 neighbor, but all other Ru-5 sites show similar energetics to the pristine slab, so no major improvement could be considered with the low Based on this, the associative mechanism (Mechanism 3) appears as the most promising one for the oxygen evolution. If Mechanism 3 is followed, the ratedetermining step (rds) appears to be the OOH* formation on the surface, which precedes oxygen evolution. For the most likely rds (Figure 7e, eq. 6, Mechanism 3, step 1), with the exception of two sites (Ru-51 site in 12.5%-5D slab and $Ru-5_1$ site in 50% slab), all other sites within the 12.5%, 25% and 50% Ti-doped structures have higher activation energies compared to RuO2. In addition, for this reaction all Ru-5 sites have lower activation energies compared to Ti-5D sites, which supports that this step of the OER occurs predominately on Ru sites rather than Ti sites. Within the proposed rds (Figure 7e), we note that two sites, Ru- 5_1 from the 25%-5/6D slab and the Ru- 5_1 from the 50% slab, have slightly lower activation energies than RuO₂.

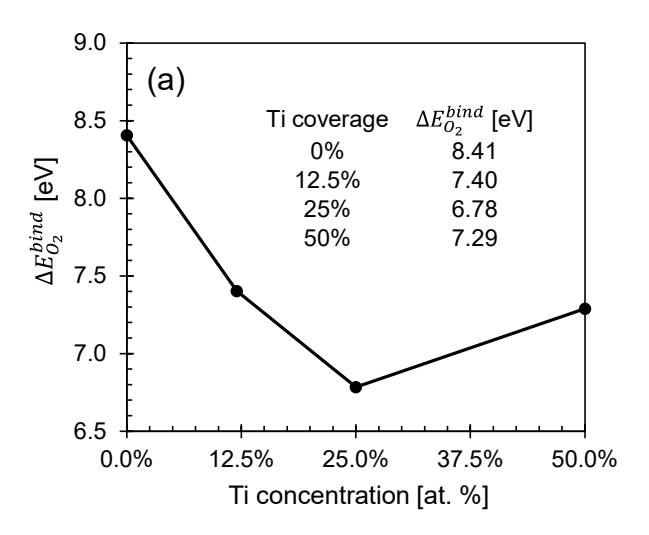
Solvation effects were also shown as very relevant in Mechanism 3 which is based on the reaction between a water molecule from the electrolyte and the surface oxygen, yielding adsorbed OOH. Evaluation of the activation barrier for such reaction on pristine RuO_2 and 12%Ti-doped RuO_2 surface (ESI, Figure S19) reveals the cooperative effects of the surface atoms. In addition, the AIMD simulations also hint to further effects of the full solvation environment on this reaction, and the subsequent OOH deprotonation. It is our aim to evaluate the main Ti effects on reactivity and stability. Additional solvation effects should be incorporated in future work.

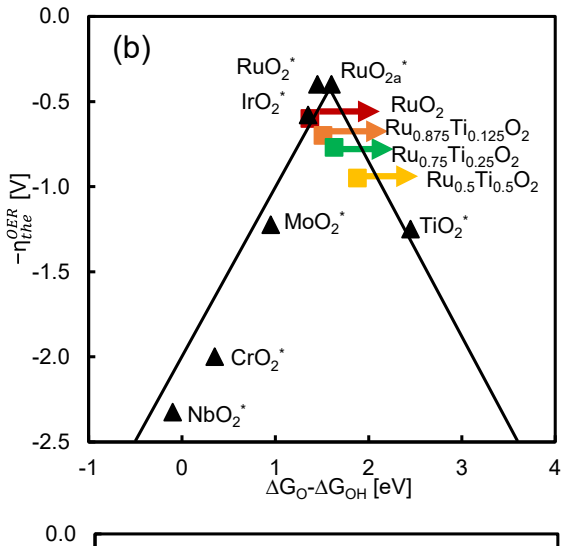
We calculated all the energy profiles for reactions involving electrons by adding the potential effect using Norskov's approach,¹¹⁵ which provides the potential effect to the reaction energies of the individual OER steps. These results, summarized in ESI, Figure S17, show the free energy of the intermediates evaluated for the pentacoordinated Ru sites on the pristine, and Ti-substituted surfaces at 12.5%-5D, 25%-5D, and 50% Ti concentration. It is concluded that for potentials of 1.23V or higher, the complete energetic pathway becomes downhill. We note however that changes in potential are tied to changes in surface composition, ³³ which will be addressed in future work.

Computational Data/Analysis Related to OER Activity and Structural Stability due to Titanium Substitution. The structural stability of transition metal electrocatalyst materials lies on the stability of M-O bonds; 116 if they are too weak it may lead to easy lattice-driven OER and structural collapse and possibly to metal dissolution. We calculated the oxygen binding energy within the bulk structure as an indicator of the M-O strength bond. Following the approach proposed by Dixit et al., 116 the oxygen binding energy corresponding to the bulk structures is obtained as function of Ti concentration, and the results are summarized in Figure 8a. The oxygen binding energy, $\Delta E_{O_2}^{bind}$, described by the following equation

$$\Delta E_{O_2}^{bind} = E_{M-O_{(defective)}} + E_{O_{2(g)}} - E_{M-O_{(perfect)}}$$

was calculated taking as reference the total energy of the bulk system with two adjacent oxygen vacancies $(E_{M-O_{(defective)}})$ obtained from removing the closest O-O pair in the structure, the energy of a gaseous oxygen molecule $(E_{O_{2(g)}})$, and the total energy of the bulk system with no vacancies $(E_{M-O_{(perfect)}})$. Note that based on this definition, $\Delta E_{O_2}^{bind}$ is related to the easiness for O_2 release from the lattice. The decrease in the binding energy of O_2 shown in Figure 8a suggests that there is a loss of M-O strength in the Ti-doped structures compared to the RuO_2 structure up to 1.63 eV, which may facilitate oxygen release via a lattice mechanism. Note that following O_2 release from the lattice, some surface reconstruction is expected to follow. Later we correlate these energies to observed changes in the electrochemical surface area.





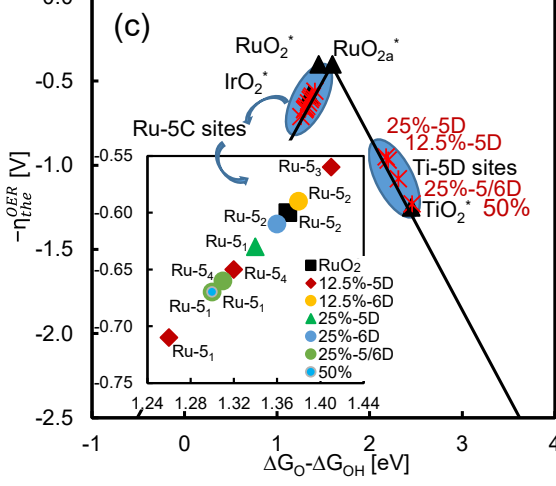


Figure 8. (a) Oxygen binding energy (eV) as function of Ti concentration in the bulk structure. There is a loss of M-O strength compared to the RuO₂ structure up to 1.63 eV in oxygen binding energy, which may induce oxygen evolution reaction from O-O interaction within the lattice; (b) average theoretical overpotential vs. activity descriptor for each concentration evaluated, (c) results from all adsorption sites evaluated on the different surface slabs; activity trend compared with previous reports from ref⁵² (black triangles):

Extrapolating the analysis to surface structures, we perform a similar examination based on the adsorption energies for neighboring O* atoms on the surfaces (ESI, Table S13) which are the negative of oxygen binding energy, suggested as an important descriptor of surface reactivity. These data show that the presence of Ti reduces the oxygen binding energy on the surface up to 1.12 eV (50% slab) and that the reduction is due to the lower adsorption energy of O* on Ti sites compared to Ru sites (ESI, Table S13). This surface dynamics helps to reduce both the activation and reaction energy for the oxygen recombination on the dopant neighboring site as discussed above, and it improves the overall surface activity for Mechanism 1 involving two specific active sites.

To complement this analysis, a second approach was followed focusing on the reactivity of adsorbed oxygen rather than that of the metal site as a key descriptor for oxidation chemistries as the OER. 110 We calculated the energy needed to deprotonate an adsorbed OH* to form adsorbed O* (step 2 in the three mechanisms), which is defined as the negative of the hydrogen binding energy on an oxygen site. This descriptor is understood as an indicative of the reactivity of the oxygen atom due to the nature of the adsorption site. Following the nomenclature proposed by Dickens et al., 110 the activity descriptor was defined as

$$\Delta E_O - \Delta E_{OH} = E_{O*} + \frac{1}{2} E_{H_{2(g)}} - E_{OH*}$$

where $\Delta E_O - \Delta E_{OH} \equiv \Delta G_O - \Delta G_{OH}$ is a commonly used OER descriptor,110 and the results are shown in ESI, Table S14. Ti sites show a considerably higher deprotonation energy compared with Ru sites (up to 60.6%, 68.6%, and 77.4% higher deprotonation energy for the 12.5%, 25%, and 50% Ti coverage, respectively, compared to the pristine RuO₂ surface), thus indicating lower metal activity. Moreover, values for Ru sites remain in a close range of 0.15 eV (maximum reduction of 8% and maximum increment of 3%), so from this descriptor the main adsorbed oxygen activity, and thus the Ru activity, appears to be independent on Ti concentration on the surface. The results agree with the study of the reaction energetics that suggested this is a thermodynamically and kinetically favorable step, with certain sites having lower activation energies than the pristine surface, and surfaces such as the 6D-showing much less improvement.

Moreover, the surface 0 atoms are crucially important as proton receptors in water splitting reactions; thus, we analyzed their effect on O-H bond strength and catalytic activity. IpCOHP analysis for both O-H* and M-O pairs with adsorbed H* are summarized in ESI, Tables S15 and S16. ESI, Table S15 displays the H* adsorption energies and pair H-O IpCOHP [eV] on surface oxygen atoms (O_B and O_t) from (110)-Ru_{1-x}Ti_xO₂ showing that adsorption is only favorable on O_B atoms, although the IpCOHP values for the H*-O_t pairs are, in average, as strong as the IpCOHP for the H*-O_B pairs for the same Ti concentrations. On the other hand, ESI, Table S16 presents the IpCOHP between the metal sites and the respective O site with adsorbed H*. Comparing their equivalent M-O pairs from ESI, Table S16, we find an important reduction on the IpCOHP strength due to the extra interaction with the adsorbed H*. Thus, IpCOHP

values for both O-H* and M-O pairs with H* adsorbed follow similar trends as obtained from surface atoms: the higher the Ti concentration the lower the IpCOHP values, and for similar concentrations the lowest IpCOHP values correspond to O-Ti bonds.

To go beyond energetics, we use the $\Delta E_O - \Delta E_{OH}$ descriptor to calculate the theoretical overpotential from DFT calculations.³² Using the relationship

$$\eta^{OER} = \{ max[(\Delta G_{O*} - \Delta G_{OH*}), 3.2 \ eV - (\Delta G_{O*} - \Delta G_{OH*})] / e \} - 1.23 \ V$$

we obtained the theoretical overpotentials plotted in Figure 8b,c (values provided in ESI, Table S14) including the data reported by Man et al.32 that established the volcanotype relationship between $\Delta G_{O*} - \Delta G_{OH*}$ and the theoretical overpotential. Prior analyses of separate RuO2 and TiO2 rutile phases using this approach determined RuO₂ binds oxygen only a little too weakly, while TiO₂ binds O* too weakly. 118 In Figure 8b, we report the overpotential vs the activity descriptor averaged for each Ti concentration. We find that at high Ti surface concentrations, the structure exhibits a higher overpotential and lower reactivity closer to the one of pristine TiO₂, whereas the values for pristine RuO2 lie in close agreement between those reported for RuO₂ and IrO₂. On the other hand, Figure 8c summarizes the data from each active site evaluated, with two groups of data related to the Ru-5 and Ti-5D sites, showing the better performance of the Ru-5 sites. Within the inset of Figure 8c we observe that two sites (Ru-53 site in the 12.5%-5D slab and Ru-5₂ site in the 12.5%-6D slab) show $\Delta G_{O*} - \Delta G_{OH*}$ values closer to the top of the volcano plot (i.e. predicted to have higher activity) compared to the best site, Ru-52, within RuO2, while the rest of the sites show values farther away from the top of the volcano plot (i.e. predicted to have lower activity). This is clear evidence of the specificity of the surface sites for maximizing activity, and of the effect of Ti on enhancing the activity of these sites. However, the existence and proportion of such active surface Ru sites depend on many other factors including synthesis, corrosion reactions, and surface restructuring, among others.

Experimental Analysis of Electrochemical Oxygen Evolution Stability. In addition to high activity, the stability of the materials under OER conditions is a key factor for long-term durability and wide-scale adoption of PEM water electrolyzers. 119 While a number of studies report Ru and RuO2 materials as the or among the most active OER catalysts, stability remains a major concern.7, 14, ¹²⁰ The stability of Ru_{1-x}Ti_xO₂ materials (x = 0, 12.5, 20 and 50 at %) was evaluated using a previously reported accelerated durability testing protocol (ADT) consisting of applying a constant potential (1.6 VRHE) over 13.5 h.9 The comparison of the current in the OER potential region, OER activity normalized by mass and surface area, Tafel slopes and ECSAs before and after ADT, are summarized in Figure 10a-e. Figure 10b corresponds to the mass activity obtained at 1.51 V_{RHE} from LSV before (initial) and after ADT (final). According to the data, RuO₂ after ADT has a significant loss of performance associated to a reduction of mass activity of 47 % from 223 to 119 mA/mg_{cat}. The reduction of mass activity of RuO2 resulted from the reduction of both ECSA and specific activity (Figure 10c,d). For the Ti-substituted

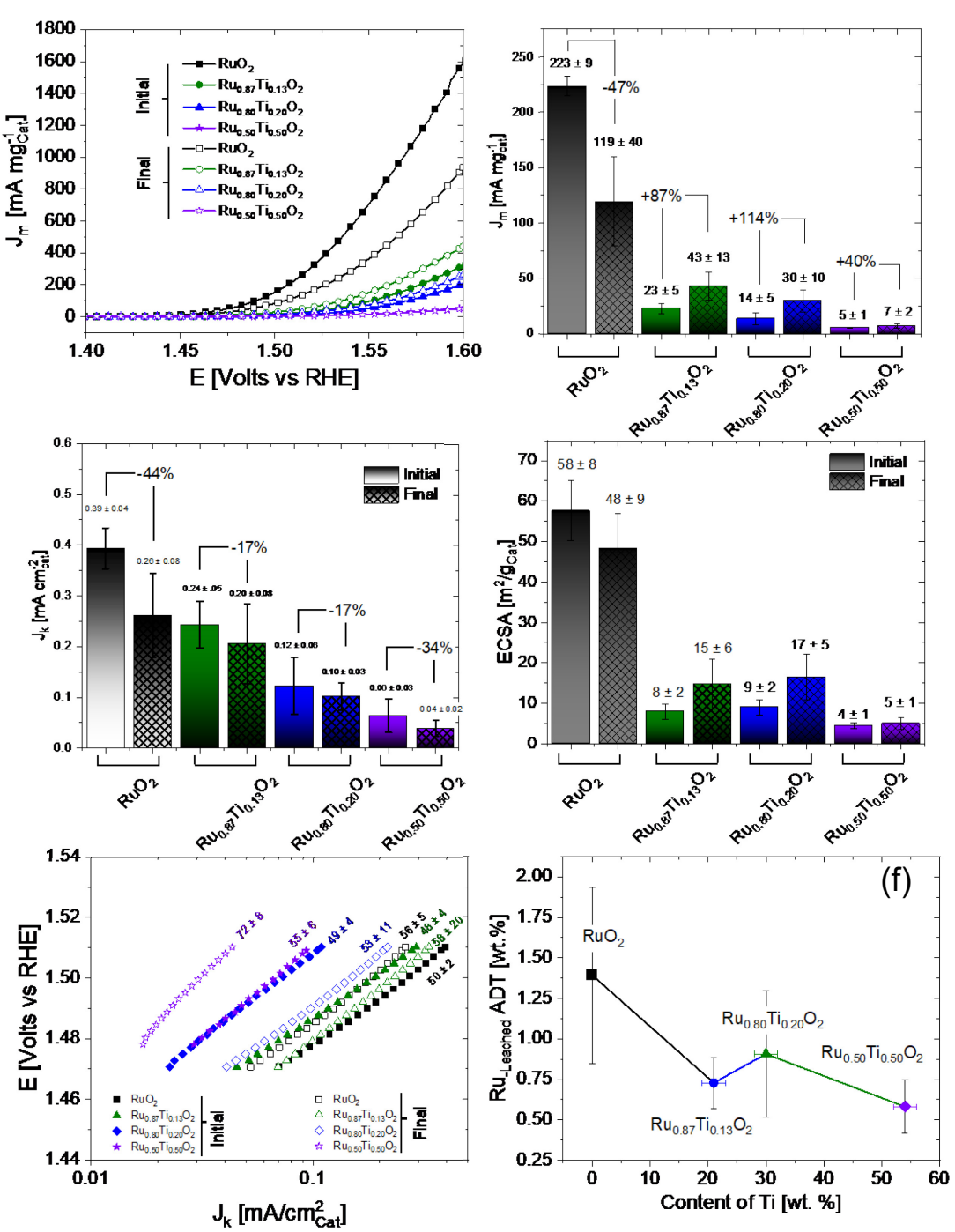


Figure 9. Comparison of oxygen evolution reaction (OER) activity, electrochemical surface area (ECSA) and Tafel slopes from initial and final (after accelerated durability testing (ADT)) measurements of RuO₂, Ru_{0.87}Ti_{0.13}O₂, Ru_{0.80}Ti_{0.20}O₂ and Ru_{0.50}Ti_{0.50}O₂; (a) current in the OER voltage region determined from linear sweep voltammetry measurements, normalized to catalyst mass; (b) comparison of initial and final OER mass activities at 1.51 V_{RHE} ; (c) comparison of initial and final OER specific activities at 1.51 V_{RHE} ; (d) comparison of initial and final ECSAs; (e) comparison of initial and final Tafel slopes; (f) relationship of percent of dissolved Ru within electrolyte after ADT determined from Inductively coupled plasma mass spectrometry (ICP-MS) measurements to atomic percent of titanium with the samples determined from EDS measurements; ADT was carried out using a potentiostatic procedure by holding the working electrode at 1.6 $V_{RHE-iR-corrected}$ for 13.5 hours under rotation at 2500 rpm in Ar-purged 0.1 M HClO₄.

samples ($Ru_{1-x}Ti_xO_2$), the OER mass activity after ADT showed a substantial increase of 40 to 114 %. The changes in mass activity can be related to multiple factors including loss of material during the electrochemical process, changes in electrochemical surface area, reduction of the specific

activity due to surface changes, changes in morphology and mass transport processes, and decreasing of conductivity, etc. From our data, the increase of the OER mass activity of nanoscale $Ru_{1-x}Ti_xO_2$ catalysts after ADT is primarily correlated to the increase of ECSA (Figure 10d), and not by

an improvement of the specific activity, which showed a slight reduction for all catalysts (Figure 10c). The opposite trends in stability observed for the Ti-substituted samples between mass activity (increases after ADT) and specific activity (decreases after ADT) underlies the importance of considering the effect of changes in surface area when evaluating stability. We note that a similar increase in activity after stability tests was reported for (Ru,Co)O2;121 however, the activity was reported on a mass basis and did not consider the changes in surface area after the stability tests. The relative reduction of specific activity was higher for RuO_2 (44 %) compared to $Ru_{1-x}Ti_xO_2$ with x=12.5 and 20 at % Ti (17 %), indicating that Ru_{1-x}Ti_xO₂ with low amounts of Ti (12.5-20 at %) resulted in improved stability compared to RuO₂. However, high amounts of Ti (50 at%) resulted in lower specific activity after ADT compared to RuO₂.

Ru dissolution from RuO₂ that occurs during OER has been previously reported. 41 Therefore, the quantification of active Ru material leached into the solution is an important parameter. The analysis of the electrochemical stability was complemented with the analysis of Ru ions leached into the solution after ADT test (Figure 10f). The RuO₂ material demonstrated the lowest stability (highest Ru dissolution) in comparison to Ru_{1-x}Ti_xO₂. This data demonstrates that the presence of Ti within the RuO2 structure stabilizes the nanoscale material against Ru dissolution, and this stabilization improves with the concentration of Ti.¹²² The Ru_{0.50}Ti_{0.50}O₂ catalyst showed both lower specific activity after ADT and the lowest Ru dissolution, which may be due to the clearly different particle shapes (ESI, Figure S2) and phase separation (Figure 3) present in the material that contribute differently to the activity and stability. In addition, we also determined that during ADT some Ti was also dissolved in the electrolyte solution (ESI, Figure S20), which may partially result from surface Ti3+ present as determined from XPS analysis (ESI, Figure S12).

The Tafel plots of RuO₂, Ru_{0.87}Ti_{0.13}O₂ and Ru_{0.80}Ti_{0.20}O₂ show the Tafel slopes slightly increased above the standard deviation after ADT (Figure 10e); however, the values remained similar to those commonly reported in literature. The similar Tafel slopes before and after ADT suggests that similar reaction mechanisms are followed after ADT. In contrast, the Ru_{0.50}Ti_{0.50}O₂ catalyst showed a major increase in its Tafel slope after ADT. A higher Ti/Ru ratio on the surface after ADT may modify the reaction mechanism, although the complexity of the system, as discussed above, requires further investigation to explain changes after ADT for the Ru_{0.50}Ti_{0.50}O₂ material. We also note that RuO₂ as well as Ru_{1-x}Ti_xO₂ may undergo significant structural changes after stability tests. A prior study of well-defined, unsubstituted RuO₂ surfaces reported significant differences after a second stability test.41

We further calculated the "stability number" (Snumber) defined as the ratio between the number of moles of evolved oxygen and dissolved catalytically active metal (in this case ruthenium), previously put forth as a metric for electrocatalyst stability, 122 and determined that introduction of Ti lowers the S-number (ESI, Figure S21). However, we also note that our stability testing was performed at 1.6 V. Higher voltages (in the range of \sim 1.7-

 $2.0\,V)$ are typical operating voltages for PEM electrolyzers, 17 and further work is needed to determine how Ti influences activity and stability at higher voltages. 113 Compared with previously reported S-numbers for Ir-based catalysts, the $Ru_{1\text{-x}}Ti_xO_2$ catalysts showed S-numbers in the range of hydrous IrO_x powders, higher S-numbers than Ba_2PrIrO_6 powder, but lower S-numbers compared to rutile $IrO_2,^{122}$ although differences in testing conditions influence the direct comparison.

A number of factors may influence the improved stability from Ti substitution. Goodenough et al. proposed that the improvement of Ru stability can be associated to changes of the oxidation potential from interaction of other metals. ¹²³ As mentioned above, the inclusion of Ti changes the electronic structure within the catalysts, which modifies the M-M and/or M-O binding energies. As shown by the discussion on the IpCOHP results (ESI, Tables S5 and S6), Ti interaction influences the strength of breaking of both surface and subsurface Ru-O bonds; however, further analysis of the effect of Ti on the Ru dissolution process is needed.

The stability results in Figure 9 may be also related to the electronic effects caused by Ti substitution in RuO₂. The Ti stabilizing effect resulting in much lower Ru dissolution can be associated to the reactivity changes found when Ti is introduced into the RuO2 structure. Signatures of less reactive surfaces were characterized by d-band center and 0-2p band center shifts away from the Fermi energy, and by higher binding energies of the O 2p electrons shown by XPS. In addition, the surface electron density distribution shows regions of electron depletion near Ti atoms and electron accumulation on top of O atoms. This electron accumulation suggests a more basic character of the Ru-O-Ti bonds. The oxidation states of surface Ru atoms are greatly altered by the introduction of Ti; even though only the pentacoordinated atoms are active sites for the catalytic reaction, both the penta- and hexa-coordinated Ru show an interesting oxidation state variation, with some Ru atoms in a higher oxidation state, and others slightly reduced. We suggest that while the penta-coordinated are active catalytic sites, the hexa-coordinated may play a role to prevent Ru dissolution. As proposed by Goodenough, 123 the metal dissolution may result from the corrosion reaction: $Ru_{oct}^{5+}O^{2-} \rightarrow (RuO_4)^{solution}$ competing with the reaction Ru_{oct}^{5+} $0^{2-} \rightarrow Ru_{oct}^{4+}0^{-}$ allowing Ru to remain on the surface acting as a catalytic site. However, if the corrosion reaction is shifted to more anodic potentials,123 then the equilibrium reaction prevails and Ru stays on the surface. Such potential shift can be produced by elements such as Ti which make the M-O bonds more basic. This basic character is given by the more negative charges on the O atoms, detected as an increasing trend as the Ti concentration increases (ESI, Table S10). Moreover, such basic sites should also be able to hold protons more tightly as found by the H-adsorption energies on the O sites of the Ti-doped surfaces (ESI, Table S15). Although Ti controls Ru dissolution, the changes observed in the ECSA denote surface reconstruction that should be given both by catalytic activity and by metal dissolution. Interestingly, the lattice O2 release inferred

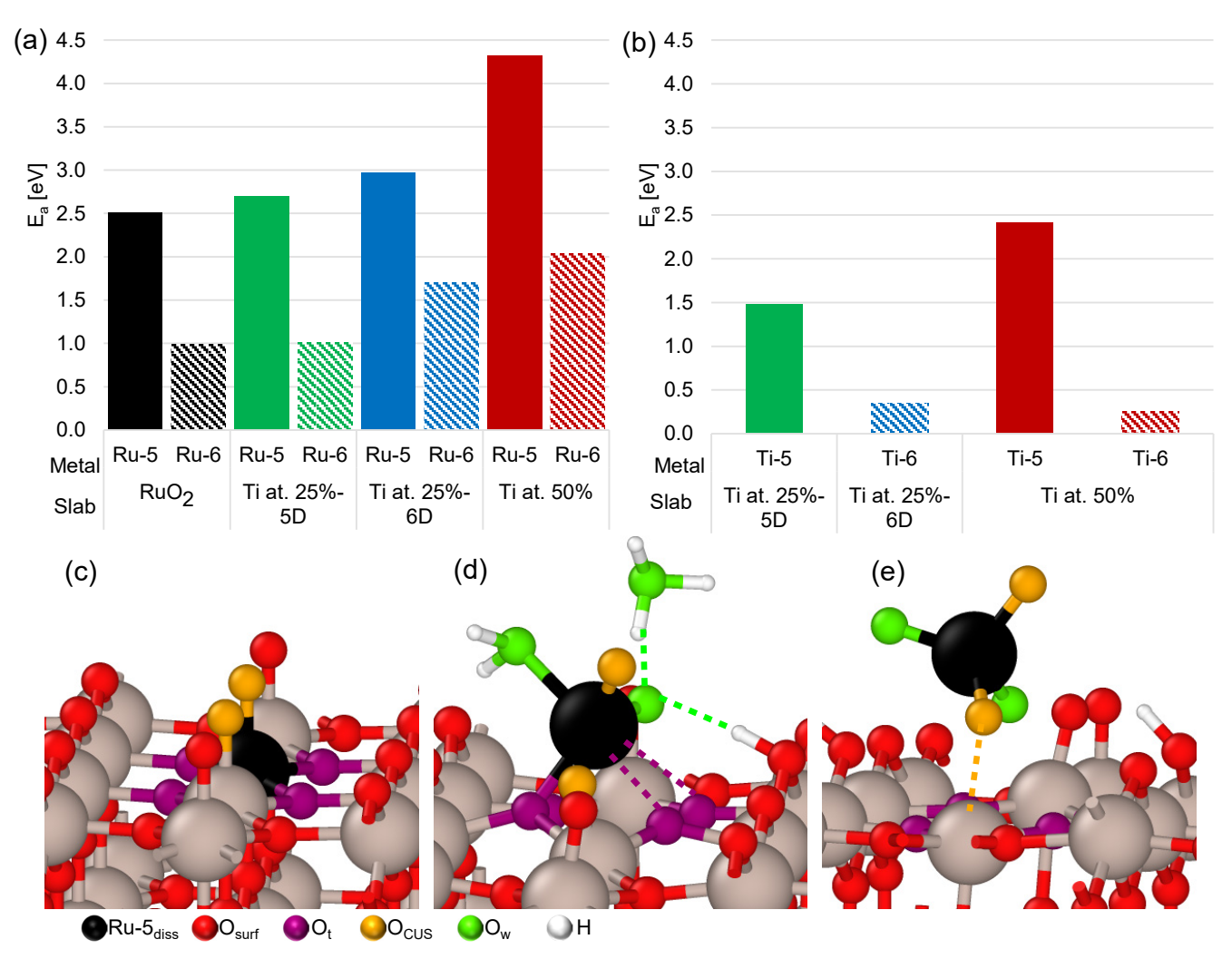


Figure 10. Top row: Activation energy necessary for dissolution of (a) Ru-penta (Ru-5) and Ru-hexa (Ru-6) coordinated, (b) Ti-penta (Ti-5) and Ti-hexa (Ti-6) coordinated breaking their main surface and subsurface O bonds. Color code for bars: black, RuO₂; green, surface with Ti at. 25% atomic concentration doped on penta-coordinated sites (Ti-5D); blue, surface with Ti at. 25% atomic concentration doped on hexa-coordinated sites (Ti-6D); red, surface with Ti at. 50%; solid bars indicate penta-coordinated metal dissolved and fading ones indicate hexa-coordinated metal dissolved. Bottom: Snapshots illustrating main events during Ru-5 dissolution: (c) initial structure, (d) Breaking of surface and subsurface O bonds followed by water bonding and oxidation, and (e) Separation of final stable RuO₄ dissolved species. Color code: black, Ru-5 dissolving; purple, O_t atoms; green, O atoms from free water molecules.

from Figure 8a shows a minimum binding (corresponding to maximum O_2 release) at 25% of Ti on the surface, which agrees with the maximum change in ECSA observed in the experiments. Thus, we speculate that the Ti concentration where the surface exhibits maximum roughness correlates with the theoretical value where O_2 tends to be the easiest to be released from the lattice.

Whether the activity and stability of OER catalysts are inherently linked or not remains a point of discussion. The predominant current thinking regarding acidic OER catalysts is that activity and stability are inherently linked since they share a common intermediate. A prior study further suggests the existence of a fundamental and universal correlation between the oxygen evolution activity and the corrosion of metal oxides based on the thermodynamic instability of the oxygen anion in the metal oxide lattice. However, other's data on oriented thin films

of RuO₂ supports that there is no correlation between OER activity and stability,41 while another study reported Ru dissolution was observed at lower potentials than OER.127 The interrelationships may be altered within metalsubstituted RuO2 where the metal substituent influences electronic structure, activity and stability. Importantly, our study shows that the effect of substitution on activity is highly dependent on the site, and specific sites may predominately act as catalytic sites for the OER, while other sites influence metal dissolution. To further investigate this point, constrained AIMD (c-AIMD) simulations were performed to evaluate dissolution of Ru and Ti surface atoms from the pristine RuO₂(110) surface and Ru_{1-x}Ti_xO₂ surfaces at 25%-5D, 25%-6D, and 50% Ti concentration. The thermodynamic integration within the slow-growth approach was used to follow the dissolution of penta- and hexa-coordinated metals on the surfaces and evaluate the

free energy pathway of the dissolving cation step by step starting from an initial configuration on the surface, until it forms a stable and fully dissolved species in the aqueous media. These simulations were carried out using the Blue Moon ensemble method as implemented in VASP. 128-132 In this way, we evaluate the activation barriers involved in the cation dissolution and identify important intermediate steps along the dissolution path. 133-135

The analyses were performed on the (110) surface, where penta- and hexa-coordinated metals have very welldefined coordination with surface and structural or subsurface oxygens. In the case of penta-coordinated atoms, the bonding interactions include one subsurface and four three-fold coordinated oxygen atoms (O_t) . The c-AIMD results indicate that the key step for penta-coordinated metal dissolution is related to the energetic barrier needed for the dissolving atom to break bonds with the structural and initial Ot oxygen atoms. On the other hand, the hexacoordinated metal atoms form bonds with two Ot atoms and four bridging or two-fold coordinated oxygen atoms (O_B), two of them being surface oxygen atoms located on the outmost part of the surface, and the other two being subsurface atoms. For the case of hexa-coordinated metals dissolution, the c-AIMD results show that the key step in the dissolution process is the breaking of the bonds of the metal with the sub surface oxygens (M-O_{Bsub}). Figure 10 summarizes the activation energies obtained for the key steps described above for the dissolution of Ru and Ti, both penta- and hexa-coordinated on RuO₂(110) pristine surface and Ru_{1-x}Ti_xO₂ surfaces at 25%-5D, 25%-6D, and 50% Ti concentration (Figure 10a and b) and shows snapshots of intermediate steps found along the dissolution path (Figure 10c to e).

Figure 10a shows that in the pristine surface, dissolution of Ru hexa-coordinated atoms (Ru-6) is considerably more favorable than that for Ru pentacoordinated (Ru-5) ones. In presence of Ti, Ru dissolution becomes less favorable (higher barriers) as the concentration of Ti increases. For example, Ru pentacoordinated dissolution exhibits an activation energy of 2.51 eV, which increases 72% up to 4.32 eV at 50% Ti concentration. At 25% Ti. the barrier for Ru-5 dissolution is 2.70 eV when Ti is located in the 5D sites, whereas in presence of Ti-6D sites the activation energy increases to 2.97 eV. In all cases there is a clear Ti effect on the barriers that translates in less Ru-5 dissolution. The activation energy for Ru hexa-coordinated atoms is considerably lower, with a value of 0.99 eV in the pristine surface. This barrier follows the exact same trend as for the pentacoordinated atoms, with the activation energy increasing as Ti concentration increases. For these cases, is clearer the effect caused by Ti-5D and -6D sites. At 25% Ti coverage, Ti-5D slightly increases the activation energy up to 1.01 eV, while the Ti-6D sites induce an increase of around 72% with an activation energy of 1.70 eV. Finally, Ti at 50% increases the activation energy more than twice, up to 2.04 eV, showing an important degree of stabilization of Ru-6 atoms against dissolution.

Figure 10b summarizes the activation energies for the key steps evaluated for the dissolution of Ti penta- and hexa-coordinated atoms. Ti dissolution exhibits a

considerably lower activation energy compared to Ru. Ti-5 exhibits activation energies of 1.48 eV and 2.41 eV in the 25%-5D and 50% slabs, respectively. Finally, Ti-6 not only exhibits the lowest dissolution activation energies overall, but also presents a different trend were its value decreases with increasing Ti concentration, as can be seen from the 0.35 eV and 0.26 eV activation energies on the 25%-6D and 50% slabs, respectively. The large barriers for Ti-5 dissolution in 50% compared with 25% are in agreement with the experimental results (ESI, Figure S20) that show less Ti dissolved at 50%, suggesting that Ti-5 may be a contributor to the leached Ti, in addition to Ti-6.

CONCLUSIONS

Using experiments and theory, we evaluated nanoscale titanium-substituted ruthenium oxide, Ru_{1-x}Ti_xO₂ (x=0-50 at %) as a model system of how the interaction of highly active, unstable metal (Ru) with a stable, relatively inactive metal (Ti) within a rutile oxide affects the atomic and electronic structure, the OER mechanism, activity and stability. Experimentally, nanoscale ruthenium-titanium oxides were synthesized using a wet chemistry route that utilized basic conditions. The computational model substituted Ti at different sites within a RuO2 (110) slab. The Ru:Ti atomic ratios within the experimentally synthesized materials are slightly higher than the nominal synthetic ratios. XRD analysis supports that the materials are predominantly (86-98%) single phase and have Ti within the rutile lattice, and a small second phase with 0-6% Ti is also present. From both experiment and theory, Ti substitution alters the crystal lattice parameters and lowers the c/a ratio.

Titanium substitution with RuO_2 alters the surface electronic structure, and the experiments and theory are in good agreement. Experimentally, the incorporation of Ti shifts core oxygen XPS and valence XPS bands (Ru 4d and 0 2p valence) to higher binding energies, and the calculated DOS shows shifting of the d-band center and 02p band center to higher binding energies. From computations, Ti substitution results in regions of electron accumulation and electron depletion within the surface, and the effects are highly dependent on specific substitution sites and Ti concentration.

The incorporation of Ti within the rutile RuO₂ structure affects the OER activity and reaction intermediates. From rotating disk electrode measurements, Ti substitution lowers the OER mass activity, OER specific activity, and ECSA. The reaction energies and activation energies of multiple OER reaction pathways (associative mechanism, direct oxygen recombination mechanism, and O and OH recombination mechanism) were evaluated on both Ru and Ti active sites using DFT, and the associative mechanism on Ru sites was determined to be the most likely reaction pathway. The effect of Ti substitution on the reaction energies and activation energies is highly dependent on the site. The correlation of the theoretical overpotential with the oxygen binding energy, commonly considered an OER descriptor, shows that substituting Ti into RuO2 increases the oxygen binding energy of some sites and decreases the oxygen binding energy of other sites, and the effect also depends on Ti concentration. At each concentration, the average oxygen binding energy over all sites predicts lower OER activity with Ti substitution, which is in line with the experimental results and suggests that the synthesized $Ru_{1-x}Ti_xO_2$ nanomaterials express predominately lower OER activity surface sites. However, calculations also indicate that at a Ti concentration of 12.5 at % results in specific sites that have an oxygen binding energy that is closer to the top of the volcano plot.

Solvation effects incorporated in the water splitting reactions with AIMD simulations. Revealed that: 1) earlier water splitting is detected on the Ti-doped surfaces compared to the pristine surfaces; 2) in all cases water splitting does not occur from the direct molecule-surface interaction but involves active presence of free water molecules, and this is a frequently observed interaction; 3) the presence of Ti sites promotes a dynamic proton exchange on the surface that favors water splitting.

In addition to affecting OER activity, titanium substitution affects the OER stability and Ru dissolution. From experimental accelerated durability testing, Ti substitution increases both the OER mass activity and the ECSA, which may be due to Ru and/or some Ti dissolution from the structure that increases surface area. When normalizing for the surface area, all Ti-substituted samples showed lower OER specific activity after the durability testing, which is the reverse trend observed for OER mass activity. Ti substitution at low and intermediate concentrations (12.5 and 20 at %) shows improved OER stability and lower Ru dissolution compared to RuO2. Interestingly, the stability and Ru dissolution for the higher Ti concentration of 50 at % was somewhat of an anomaly since this material showed lower OER stability compared with RuO2, but also lower Ru dissolution, which may result from the different particle morphologies within the material that contribute differently to these processes. Overall, experimentally we find that Ti substitution within RuO₂ at low and intermediate concentrations lowers the OER specific activity and increases the stability. The results obtained at high Ti concentration support that higher concentration of Ti does not necessarily inherently further improve stability, but that the effect of Ti on the OER activity and stability or RuO₂ depends on the Ti concentration, synthesis route, and how the metal incorporates within the surface.

Analysis of stability from calculations indicates that Ti substitution improves stability and also suggests that the effect of Ti substitution on stability is also highly sitespecific: there may be sites that contribute to OER while other sites are involved in Ru dissolution. The role of Ti on reducing barriers for Ru dissolution is shown clearly from the c-AIMD simulations. Dissolution of Ru hexa-coordinated atoms is considerably more favorable than that for Ru penta-coordinated ones. In the presence of Ti, Ru dissolution becomes less favorable (higher barriers) as the concentration of Ti increases, which is in agreement with the experimental results that show Ti substitution with RuO2 lowers the amount of dissolved Ru and therefore improves stability. Comparing the most probable sites for OER (penta-coordinated Ru) and dissolution (hexacoordinated Ru), OER and dissolution occur at different sites. We consider that activity and stability may be coupled to some extent; however, different sites may affect activity and stability and the effects depend on the metal substituent, site, and concentration. The understanding how specific sites influence electronic structure, activity and stability provides a design strategy to obtain higher activity, improved stability and lower cost OER electrocatalysts.

ASSOCIATED CONTENT

Supporting Information. Additional calculations and experiments on RuO_2 and $Ru_{1-x}Ti_xO_2$ (x=0–50 at %): Hubbard U parameter calculations, SEM images, EDS mapping, pore-size distributions, X-ray diffraction, lattice parameters, pair radial distribution functions, X-ray photoelectron spectroscopy, calculated DOS, Bader charges, electrochemical testing, reaction, activation and adsorption energies, AIMD analysis, metal dissolution. This material is available free of charge via the Internet at http://pubs.acs.org.

AUTHOR INFORMATION

Corresponding Authors

* email: cprhodes@txstate.edu; Phone: 512-245-6721. Fax: 512-245-2374; orcid.org/0000-0003-4886-9875

*email: balbuena@tamu.edu; Phone: 979-845-3375 · Fax: 979-845-6446; orcid.org/0000-0002-2358-3910

Author Contributions

‡These authors contributed equally to this work. All authors contributed to the analysis of the results and writing of the manuscript.

Notes

The authors declare no competing financial interests or other conflicts of interest.

ACKNOWLEDGMENT

The authors acknowledge support of this research from the National Science Foundation (NSF) Award No. 1936458 and 1936495. P.B.B and F.O.A gratefully acknowledge supercomputer resources from the Texas A&M University High Performance Research Computing Center. K.B. acknowledges support from the NSF Research Experiences for Undergraduates (REU) program, Award No. 1757843, for corelevel XPS analysis. C.P.R., L.A. and K.B. acknowledge support from NSF Partnerships for Research and Education in Materials (PREM) Center for Intelligent Materials Assembly (CIMA), Award No. 2122041 for valence-level XPS analysis.

REFERENCES

- 1. Spori, C.; Kwan, J. T. H.; Bonakdarpour, A.; Wilkinson, D. P.; Strasser, P., The Stability Challenges of Oxygen Evolving Catalysts: Towards a Common Fundamental Understanding and Mitigation of Catalyst Degradation. *Angew. Chem.-Int. Edit.* **2017**, *56* (22), 5994-6021.
- 2. Alia, S.; Ding, D.; McDaniel, A.; Toma, F. M.; Dinh, H. N., How to Make Clean Hydrogen AWSM: The Advanced Water Splitting Materials Consortium. *Electrochem. Soc. Interface* **2021**, *30* (4), 50-56.
- 3. Fabbri, E.; Habereder, A.; Waltar, K.; Kotz, R.; Schmidt, T. J., Developments and perspectives of oxide-based catalysts for the oxygen evolution reaction. *Catal. Sci. Technol.* **2014**, *4* (11), 3800-3821.

- 4. Reier, T.; Nong, H. N.; Teschner, D.; Schlogl, R.; Strasser, P., Electrocatalytic Oxygen Evolution Reaction in Acidic Environments Reaction Mechanisms and Catalysts. *Adv. Energy Mater.* **2017**, *7* (1).
- 5. Suen, N. T.; Hung, S. F.; Quan, Q.; Zhang, N.; Xu, Y. J.; Chen, H. M., Electrocatalysis for the oxygen evolution reaction: recent development and future perspectives. *Chem. Soc. Rev.* **2017**, *46* (2), 337-365.
- 6. Danilovic, N.; Subbaraman, R.; Chang, K. C.; Chang, S. H.; Kang, Y. J. J.; Snyder, J.; Paulikas, A. P.; Strmcnik, D.; Kim, Y. T.; Myers, D.; Stamenkovic, V. R.; Markovic, N. M., Activity-Stability Trends for the Oxygen Evolution Reaction on Monometallic Oxides in Acidic Environments. *J. Phys. Chem. Lett.* **2014**, *5* (14), 2474-2478.
- 7. Reier, T.; Oezaslan, M.; Strasser, P., Electrocatalytic Oxygen Evolution Reaction (OER) on Ru, Ir, and Pt Catalysts: A Comparative Study of Nanoparticles and Bulk Materials. *ACS Catal.* **2012**, *2* (8), 1765-1772.
- 8. McCrory, C. C. L.; Jung, S.; Ferrer, I. M.; Chatman, S. M.; Peters, J. C.; Jaramillo, T. F., Benchmarking Hydrogen Evolving Reaction and Oxygen Evolving Reaction Electrocatalysts for Solar Water Splitting Devices. *J. Am. Chem. Soc.* **2015**, *137* (13), 4347-4357.
- 9. Alia, S. M.; Shulda, S.; Ngo, C.; Pylypenko, S.; Pivovar, B. S., Iridium-Based Nanowires as Highly Active, Oxygen Evolution Reaction Electrocatalysts. *ACS Catal.* **2018**, δ (3), 2111-2120.
- 10. Alia, S. M.; Rasimick, B.; Ngo, C.; Neyerlin, K. C.; Kocha, S. S.; Pylypenko, S.; Xu, H.; Pivovar, B. S., Activity and Durability of Iridium Nanoparticles in the Oxygen Evolution Reaction. *J. Electrochem. Soc.* **2016**, *163* (11), F3105-F3112.
- 11. Godínez-Salomón, F.; Albiter, L.; Alia, S.; Pivovar, B.; Forero, L. C.; Balbuena, P.; Mendoza-Cruz, R.; Arellano-Jimenez, M. J.; Rhodes, C. P., Self-Supported Hydrous Iridium-Nickel Oxide Two-dimensional Nanoframes for High Activity Oxygen Evolution Electrocatalysts. *ACS Catal.* **2018**, *8*, 10498-10520.
- 12. Ying, Y. F.; Salomon, J. F. G.; Lartundo-Rojas, L.; Moreno, A.; Meyer, R.; Damin, C. A.; Rhodes, C. P., Hydrous cobalt-iridium oxide two-dimensional nanoframes: insights into activity and stability of bimetallic acidic oxygen evolution electrocatalysts. *Nanoscale Adv.* **2021**, *3* (7), 1976-1996.
- 13. Lee, Y.; Suntivich, J.; May, K. J.; Perry, E. E.; Shao-Horn, Y., Synthesis and Activities of Rutile IrO₂ and RuO₂ Nanoparticles for Oxygen Evolution in Acid and Alkaline Solutions. *J. Phys. Chem. Lett.* **2012**, *3* (3), 399-404.
- 14. Cherevko, S.; Geiger, S.; Kasian, O.; Kulyk, N.; Grote, J. P.; Savan, A.; Shrestha, B. R.; Merzlikin, S.; Breitbach, B.; Ludwig, A.; Mayrhofer, K. J. J., Oxygen and hydrogen evolution reactions on Ru, RuO₂, Ir, and IrO₂ thin film electrodes in acidic and alkaline electrolytes: A comparative study on activity and stability. *Catal. Today* **2016**, *262*, 170-180.
- 15. Park, J. W.; Hu, Z. C.; Gao, S.; Campbell, I. H.; Gong, H. J., Platinum group element abundances in the upper continental crust revisited New constraints from analyses of Chinese loess. *Geochim. Cosmochim. Acta* **2012**, *93*, 63-76.
- 16. U.S. Geological Survey Platinum-Group Metals Statistics and Information https://minerals.usgs.gov/minerals/pubs/commodity/platinum/. (accessed February 2, 2022).

- 17. Alia, S. M., Current research in low temperature proton exchange membrane-based electrolysis and a necessary shift in focus. *Curr. Opin. Chem. Eng.* **2021**, *33*, 100703.
- 18. Gloag, L.; Benedetti, T. M.; Cheong, S.; Li, Y. B.; Chan, X. H.; Lacroix, L. M.; Chang, S. L. Y.; Arenal, R.; Florea, I.; Barron, H.; Barnard, A. S.; Henning, A. M.; Zhao, C.; Schuhmann, W.; Gooding, J. J.; Tilley, R. D., Three-Dimensional Branched and Faceted Gold-Ruthenium Nanoparticles: Using Nanostructure to Improve Stability in Oxygen Evolution Electrocatalysis. *Angew. Chem.-Int. Edit.* **2018**, *57* (32), 10241-10245.
- 19. Zhang, Q.; Kusada, K.; Wu, D. S.; Kawaguchi, S.; Kubota, Y.; Kitagawa, H., Crystal Structure-dependent Thermal Stability and Catalytic Performance of AuRu3 Solid-solution Alloy Nanoparticles. *Chem. Lett.* **2018**, *47* (4), 559-561
- 20. Puthiyapura, V. K.; Pasupathi, S.; Basu, S.; Wu, X.; Su, H. N.; Varagunapandiyan, N.; Pollet, B.; Scott, K., Ru_xNb_{1-x}O₂ catalyst for the oxygen evolution reaction in proton exchange membrane water electrolysers. *Int. J. Hydrog. Energy* **2013**, *38* (21), 8605-8616.
- 21. Danilovic, N.; Subbaraman, R.; Chang, K. C.; Chang, S. H.; Kang, Y. J.; Snyder, J.; Paulikas, A. P.; Strmcnik, D.; Kim, Y. T.; Myers, D.; Stamenkovic, V. R.; Markovic, N. M., Using Surface Segregation To Design Stable Ru-Ir Oxides for the Oxygen Evolution Reaction in Acidic Environments. *Angew. Chem.-Int. Edit.* **2014**, *53* (51), 14016-14021.
- 22. Gloag, L.; Benedetti, T. M.; Cheong, S.; Webster, R. F.; Marjo, C. E.; Gooding, J. J.; Tilley, R. D., Pd-Ru coreshell nanoparticles with tunable shell thickness for active and stable oxygen evolution performance. *Nanoscale* **2018**, *10* (32), 15173-15177.
- 23. Lin, Y. C.; Tian, Z. Q.; Zhang, L. J.; Ma, J. Y.; Jiang, Z.; Deibert, B. J.; Ge, R. X.; Chen, L., Chromium-ruthenium oxide solid solution electrocatalyst for highly efficient oxygen evolution reaction in acidic media. *Nat. Commun.* **2019**, *10*, 13.
- 24. Kim, J.; Shih, P. C.; Tsao, K. C.; Pan, Y. T.; Yin, X.; Sun, C. J.; Yang, H., High-Performance Pyrochlore-Type Yttrium Ruthenate Electrocatalyst for Oxygen Evolution Reaction in Acidic Media. *J. Am. Chem. Soc.* **2017**, *139* (34), 12076-12083.
- 25. Kim, J.; Shih, P. C.; Qin, Y.; Al-Bardan, Z.; Sun, C. J.; Yang, H., A Porous Pyrochlore Y-2 Ru1.6Y0.4 O7-delta Electrocatalyst for Enhanced Performance towards the Oxygen Evolution Reaction in Acidic Media. *Angew. Chem.-Int. Edit* **2018**, *57* (42), 13877-13881.
- 26. Yao, Y. C.; Hu, S. L.; Chen, W. X.; Huang, Z. Q.; Wei, W. C.; Yao, T.; Liu, R. R.; Zang, K. T.; Wang, X. Q.; Wu, G.; Yuan, W. J.; Yuan, T. W.; Zhu, B. Q.; Liu, W.; Li, Z. J.; He, D. S.; Xue, Z. G.; Wang, Y.; Zheng, X. S.; Dong, J. C.; Chang, C. R.; Chen, Y. X.; Hong, X.; Luo, J.; Wei, S. Q.; Li, W. X.; Strasser, P.; Wu, Y. E.; Li, Y. D., Engineering the electronic structure of single atom Ru sites via compressive strain boosts acidic water oxidation electrocatalysis. *Nat. Catal.* **2019**, *2* (4), 304-313.
- 27. DeSario, P. A.; Chervin, C. N.; Nelson, E. S.; Sassin, M. B.; Rolison, D. R., Competitive Oxygen Evolution in Acid Electrolyte Catalyzed at Technologically Relevant Electrodes Painted with Nanoscale RuO₂. *ACS Appl. Mater. Interfaces* **2017**, *9* (3), 2387-2395.
- 28. Kanno, R.; Murayama, M.; Inada, T.; Kobayashi, T.; Sakamoto, K.; Sonoyama, N.; Yamada, A.; Kondo, S., A self-

- assembled breathing interface for all-solid-state ceramic lithium batteries. *Electrochem. Solid State Lett.* **2004,** 7 (12), A455-A458
- 29. Chen, Z. J.; Duan, X. G.; Wei, W.; Wang, S. B.; Ni, B. J., Iridium-based nanomaterials for electrochemical water splitting. *Nano Energy* **2020**, *78*, 28.
- 30. Shi, Q. R.; Zhu, C. Z.; Du, D.; Lin, Y. H., Robust noble metal-based electrocatalysts for oxygen evolution reaction. *Chem. Soc. Rev.* **2019**, *48* (12), 3181-3192.
- 31. Song, J. J.; Wei, C.; Huang, Z. F.; Liu, C. T.; Zeng, L.; Wang, X.; Xu, Z. C. J., A review on fundamentals for designing oxygen evolution electrocatalysts. *Chem. Soc. Rev.* **2020**, *49* (7), 2196-2214.
- 32. Man, I. C.; Su, H. Y.; Calle-Vallejo, F.; Hansen, H. A.; Martínez, J. I.; Inoglu, N. G.; Kitchin, J.; Jaramillo, T. F.; Nørskov, J. K.; Rossmeisl, J., Universality in Oxygen Evolution Electrocatalysis on Oxide Surfaces. *ChemCatChem* **2011**, *3* (7), 1159-1165.
- 33. Rao, R. R.; Kolb, M. J.; Halck, N. B.; Pedersen, A. F.; Mehta, A.; You, H.; Stoerzinger, K. A.; Feng, Z.; Hansen, H. A.; Zhou, H.; Giordano, L.; Rossmeisl, J.; Vegge, T.; Chorkendorff, I.; Stephens, I. E. L.; Shao-Horn, Y., Towards identifying the active sites on RuO₂(110) in catalyzing oxygen evolution. *Energy Environ. Sci.* **2017**, *10* (12), 2626-2637.
- 34. Wohlfahrt-Mehrens, M.; Heitbaum, J., Oxygen evolution on Ru and RuO₂ electrodes studied using isotope labelling and on-line mass spectrometry. *Journal of Electroanalytical Chemistry and Interfacial Electrochemistry* **1987**, 237 (2), 251-260.
- 35. Stoerzinger, K. A.; Diaz-Morales, O.; Kolb, M.; Rao, R. R.; Frydendal, R.; Qiao, L.; Wang, X. R.; Halck, N. B.; Rossmeisl, J.; Hansen, H. A.; Vegge, T.; Stephens, I. E. L.; Koper, M. T. M.; Shao-Horn, Y., Orientation-Dependent Oxygen Evolution on RuO₂ without Lattice Exchange. *ACS Energy Lett.* **2017**, *2* (4), 876-881.
- 36. González, D.; Heras-Domingo, J.; Pantaleone, S.; Rimola, A.; Rodríguez-Santiago, L.; Solans-Monfort, X.; Sodupe, M., Water Adsorption on MO₂ (M = Ti, Ru, and Ir) Surfaces. Importance of Octahedral Distortion and Cooperative Effects. *ACS Omega* **2019**, *4* (2), 2989-2999.
- 37. Klyukin, K.; Zagalskaya, A.; Alexandrov, V., Role of Dissolution Intermediates in Promoting Oxygen Evolution Reaction at RuO₂(110) Surface. *J. Phys. Chem. C* **2019**, *123* (36), 22151-22157.
- 38. Zagalskaya, A.; Alexandrov, V., Role of Defects in the Interplay between Adsorbate Evolving and Lattice Oxygen Mechanisms of the Oxygen Evolution Reaction in RuO₂ and IrO₂. ACS Catalysis **2020**, 10 (6), 3650-3657.
- 39. Zagalskaya, A.; Alexandrov, V., Mechanistic Study of IrO2 Dissolution during the Electrocatalytic Oxygen Evolution Reaction. *The Journal of Physical Chemistry Letters* **2020**, *11* (7), 2695-2700.
- 40. García-Mota, M.; Vojvodic, A.; Metiu, H.; Man, I. C.; Su, H. Y.; Rossmeisl, J.; Nørskov, J. K., Tailoring the Activity for Oxygen Evolution Electrocatalysis on Rutile TiO₂ (110) by Transition-Metal Substitution. *ChemCatChem* **2011**, *3* (10), 1607-1611.
- 41. Roy, C.; Rao, R. R.; Stoerzinger, K. A.; Hwang, J.; Rossmeisl, J.; Chorkendorff, I.; Shao-Horn, Y.; Stephens, I. E. L., Trends in Activity and Dissolution on RuO₂ under Oxygen Evolution Conditions: Particles versus Well-Defined Extended Surfaces. *ACS Energy Lett.* **2018**, *3* (9), 2045-2051.

- 42. Petrykin, V.; Macounova, K.; Franc, J.; Shlyakhtin, O.; Klementova, M.; Mukerjee, S.; Krtil, P., Zn-Doped RuO₂ electrocatalyts for Selective Oxygen Evolution: Relationship between Local Structure and Electrocatalytic Behavior in Chloride Containing Media. *Chem. Mater.* **2011**, *23* (2), 200-207.
- 43. Chen, S.; Huang, H.; Jiang, P.; Yang, K.; Diao, J. F.; Gong, S. P.; Liu, S.; Huang, M. X.; Wang, H.; Chen, Q. W., Mn-Doped RuO₂ Nanocrystals as Highly Active Electrocatalysts for Enhanced Oxygen Evolution in Acidic Media. *ACS Catal.* **2020**, *10* (2), 1152-1160.
- 44. Wu, Y. Y.; Tariq, M.; Zaman, W. Q.; Sun, W.; Zhou, Z. H.; Yang, J., Bimetallic Doped RuO2 with Manganese and Iron as Electrocatalysts for Favorable Oxygen Evolution Reaction Performance. *ACS Omega* **2020**, *5* (13), 7342-7347.
- 45. Gonzalez-Huerta, R. G.; Ramos-Sanchez, G.; Balbuena, P. B., Oxygen evolution in Co-doped RuO₂ and IrO₂: Experimental and theoretical insights to diminish electrolysis overpotential. *J. Power Sources* **2014**, *268*, 69-76.
- 46. Contu, F.; Elsener, B.; Bohni, H., Electrochemical behavior of CoCrMo alloy in the active state in acidic and alkaline buffered solutions. *J. Electrochem. Soc.* **2003**, *150* (9), B419-B424.
- 47. Muller, A.; Popkirov, G. S.; Schindler, R. N., The Anodic Growth and the Stability of Thin Passive Films on Titanium Electrodes. *Phys. Chem. Chem. Phys.* **1992**, *96* (10), 1432-1437.
- 48. Kasian, O.; Li, T.; Mingers, A. M.; Schweinar, K.; Savan, A.; Ludwig, A.; Mayrhofer, K., Stabilization of an iridium oxygen evolution catalyst by titanium oxides. *J. Phys. Energy* **2021**, *3* (3).
- 49. Frisch, M.; Raza, M. H.; Ye, M. Y.; Sachse, R.; Paul, B.; Gunder, R.; Pinna, N.; Kraehnert, R., ALD-Coated Mesoporous Iridium-Titanium Mixed Oxides: Maximizing Iridium Utilization for an Outstanding OER Performance. *Adv. Mater. Interface* **2022**, *9* (6).
- 50. Menzel, N.; Ortel, E.; Mette, K.; Kraehnert, R.; Strasser, P., Dimensionally Stable Ru/Ir/TiO2-Anodes with Tailored Mesoporosity for Efficient Electrochemical Chlorine Evolution. *ACS Catal.* **2013**, *3* (6), 1324-1333.
- 51. Naslund, L. A.; Sanchez-Sanchez, C. M.; Ingason, A. S.; Backstrom, J.; Herrero, E.; Rosen, J.; Holmin, S., The Role of TiO₂ Doping on RuO₂-Coated Electrodes for the Water Oxidation Reaction. *J. Phys. Chem. C* **2013**, *117* (12), 6126-6135
- 52. Kishor, K.; Saha, S.; Gupta, M. K.; Bajpai, A.; Chatterjee, M.; Sivakumar, S.; Pala, R. G. S., Roughened Zn-Doped Ru-Ti Oxide Water Oxidation Electrocatalysts by Blending Active and Activated Passive Components. *ChemElectroChem* **2015**, *2* (11), 1839-1846.
- 53. Swider, K. E.; Merzbacher, C. I.; Hagans, P. L.; Rolison, D. R., Synthesis of ruthenium dioxide titanium dioxide aerogels: Redistribution of electrical properties on the nanoscale. *Chem. Mat.* **1997**, *9* (5), 1248-1255.
- 54. Hu, C. C.; Yang, Y. L.; Lee, T. C., Microwave-Assisted Hydrothermal Synthesis of RuO₂ · xH₂O-TiO₂ Nanocomposites for High Power Supercapacitors. *Electrochem. Solid State Lett.* **2010,** *13* (12), A173-A176.
- 55. Guglielmi, M.; Colombo, P.; Rigato, V.; Battaglin, G.; Boscoloboscoletto, A.; Debattisti, A., Composition and Microstructural Characterization of RuO₂-TiO₂ Catalysts Synthesized by the Sol-Gel Method. *J. Electrochem. Soc.* **1992**, *139* (6), 1655-1661.

- 56. Kameyama, K.; Shohji, S.; Onoue, S.; Nishimura, K.; Yahikozawa, K.; Takasu, Y., Preparation of Ultrafine RuO₂-TiO₂ Binary Oxide Particles by a Sol-Gel Process. *J. Electrochem. Soc.* **1993**, *140* (4), 1034-1037.
- 57. Haas, O. E.; Briskeby, S. T.; Kongstein, O. E.; Tsypkin, M.; Tunold, R.; Borresen, B. T., Synthesis and characterisation of Ru_xTi_{x-1}O₂ as a catalyst support for polymer electrolyte fuel cell. *Journal of New Materials for Electrochemical Systems* **2008**, *11* (1), 9-14.
- 58. Malek, J.; Watanabe, A.; Mitsuhashi, T., Sol-gel preparation of rutile type solid solution in TiO₂-RuO₂ system. *J. Therm. Anal.* **2000**, *60* (2), 699-705.
- 59. Roginskaya, Y. E.; Morozova, O. V., The role of hydrated oxides in formation and structure of DSA-type oxide electrocatalysts. *Electrochim. Acta* **1995**, *40* (7), 817-822.
- 60. Duvigneaud, P. H.; Coussement, A., Effect of Chlorine on Solid-Slution Formation in Ruthenium Titanium-Dioxide Coatings. *J. Solid State Chem.* **1984**, *52* (1), 22-31.
- 61. Gaudet, J.; Tavares, A. C.; Trasatti, S.; Guay, D., Physicochemical characterization of mixed RuO₂-SnO₂ solid solutions. *Chem. Mat.* **2005**, *17* (6), 1570-1579.
- 62. Colomer, M. T.; Jurado, J. R., Structural, microstructural, and electrical transport properties of TiO₂-RuO₂ ceramic materials obtained by polymeric sol-gel route. *Chem. Mat.* **2000**, *12* (4), 923-930.
- 63. Rogers, D. B.; Shannon, R. D.; Sleight, A. W.; Gillson, J. L., Crystal chemistry of metal dioxides with rutile-related structures. *Inorg. Chem.* **1969**, *8* (4), 841-849.
- 64. McCafferty, L.; O'Rourke, C.; Mills, A.; Kafizas, A.; Parkin, I. P.; Darr, J. A., Light-driven generation of chlorine and hydrogen from brine using highly selective Ru/Ti oxide redox catalysts. *Sustain. Energy Fuels* **2017**, *1* (2), 254-257.
- 65. Butler, S. R.; Gillson, J. L., Crystal growth, electrical resistivity and lattice parameters of RuO₂ and IrO₂. *Mater. Res. Bull.* **1971**, *6* (2), 81-89.
- 66. Huang, Y. S.; Park, H. L.; Pollak, F. H., Growth and characterization of RuO₂ single crystals. *Mater. Res. Bull.* **1982**, *17* (10), 1305-1312.
- 67. Wang, X.; Shao, Y. Q.; Liu, X. H.; Tang, D. A.; Wu, B.; Tang, Z. Z.; Wang, X.; Lin, W., Phase Stability and Phase Structure of Ru-Ti-O Complex Oxide Electrocatalyst. *J. Amer. Ceram. Soc.* **2015**, *98* (6), 1915-1924.
- 68. Hamad, B. A., First-principle calculations of structural and electronic properties of rutile-phase dioxides (MO₂), M = Ti, V, Ru, Ir and Sn. *Eur. Phys. J. B* **2009**, *70* (2), 163-169.
- 69. Wang, X.; Shao, Y. Q.; Liu, X. H.; Tang, D. A.; Wu, B.; Tang, Z. Z.; Wang, X.; Lin, W., Phase Stability and Phase Structure of Ru-Ti-O Complex Oxide Electrocatalyst. *J. Amer. Ceram. Soc.* **2015**, *98* (6), 1915-1924.
- 70. Shannon, R. D., Revised Effective Ionic Radii and Systematic Studies of Interatomic Distances in Halides and Chalcogenides. *Acta Cryst. A* **1976**, *32*, 751-767.
- 71. Zakaryan, H. A.; Kvashnin, A. G.; Oganov, A. R., Stable reconstruction of the (110) surface and its role in pseudocapacitance of rutile-like RuO₂. *Sci. Rep.* **2017**, *7* (1), 10357.
- 72. Gemming, S.; Enyashin, A. N.; Frenzel, J.; Seifert, G., Adsorption of nucleotides on the rutile (110) surface. *Int. J. Mater. Res.* **2010**, *101* (6), 758-764.
- 73. Reuter, K.; Scheffler, M., Composition, structure, and stability of RuO₂ as a function of oxygen pressure. *Phys. Rev. B* **2001**, *65* (3), 035406.

- 74. Henrich, V. E.; Cox, P. A., *The Surface Science of Metal Oxides*. Cambridge University Press: 1996.
- 75. Noguera, C., *Physics and Chemistry at Oxide Surfaces*. Cambridge University Press: 1996.
- 76. Dickens, C. F.; Nørskov, J. K., A Theoretical Investigation into the Role of Surface Defects for Oxygen Evolution on RuO₂. *J. Phys. Chem. C* **2017**, *121* (34), 18516-18524
- 77. Kim, Y. D.; Seitsonen, A. P.; Wendt, S.; Wang, J.; Fan, C.; Jacobi, K.; Over, H.; Ertl, G., Characterization of Various Oxygen Species on an Oxide Surface: RuO₂(110). *J. Phys. Chem. B* **2001**, *105* (18), 3752-3758.
- 78. Over, H., Surface Chemistry of Ruthenium Dioxide in Heterogeneous Catalysis and Electrocatalysis: From Fundamental to Applied Research. *Chem. Rev.* **2012**, *112* (6), 3356-3426.
- 79. Rao, R. R.; Kolb, M. J.; Halck, N. B.; Pedersen, A. F.; Mehta, A.; You, H.; Stoerzinger, K. A.; Feng, Z. X.; Hansen, H. A.; Zhou, H.; Giordano, L.; Rossmeisl, J.; Vegge, T.; Chorkendorff, I.; Stephens, I. E. L.; Shao-Horn, Y., Towards identifying the active sites on RuO₂(110) in catalyzing oxygen evolution. *Energy Environ. Sci.* **2017**, *10* (12), 2626-2637.
- 80. Riga, J.; Tenretnoel, C.; Pireaux, J. J.; Caudano, R.; Verbist, J. J.; Gobillon, Y., Electronic Structure of Rutile Oxides TiO₂, RuO₂, and IrO₂ Studied by X-ray Photoelectron Spectroscopy. *Phys. Scr.* **1977**, *16* (5-6), 351-354.
- 81. Morgan, D. J., Resolving ruthenium: XPS studies of common ruthenium materials. *Surf. Interface Anal.* **2015**, *47* (11), 1072-1079.
- 82. Biesinger, M. C.; Lau, L. W. M.; Gerson, A. R.; Smart, R. S. C., Resolving surface chemical states in XPS analysis of first row transition metals, oxides and hydroxides: Sc, Ti, V, Cu and Zn. *Appl. Surf. Sci.* **2010**, *257* (3), 887-898.
- 83. Nasser, S. A., X-ray photoelectron spectroscopy study on the composition and structure of BaTiO3 thin films deposited on silicon. *Appl. Surf. Sci.* **2000**, *157* (1-2), 14-22.
- 84. Goodenough, J. B., The Two Components of the Crystallographic Transition in VO₂. *J. Solid State Chem.* **1971**, *3* (4), 490-500.
- 85. Cox, P. A.; Goodenough, J. B.; Tavener, P. J.; Telles, D.; Egdell, R. G., The Electronic Stucture of Bi_{2-x}GdRu₂O₇ and RuO₂: A Study by Electron Spectroscopy *J. Solid State Chem.* **1986**, *62* (3), 360-370.
- 86. Kahk, J. M.; Poll, C. G.; Oropeza, F. E.; Ablett, J. M.; Geolin, D.; Rueff, J. P.; Agrestini, S.; Utsumi, Y.; Tsuei, K. D.; Liao, Y. F.; Borgatti, F.; Panaccione, G.; Regoutz, A.; Egdell, R. G.; Morgan, B. J.; Scanlon, D. O.; Payne, D. J., Understanding the Electronic Structure of IrO₂ Using Hard-X-ray Photoelectron Spectroscopy and Density-Functional Theory. *Phys. Rev. Lett.* **2014**, *112* (11).
- 87. Li, K. Y.; Xue, D. F., Estimation of electronegativity values of elements in different valence states. *J. Phys. Chem. A* **2006**, *110* (39), 11332-11337.
- 88. Handbook of Heterogeneous Catalysis. VCH Verlagsgesellschaft: Berlin, 1997.
- 89. Benyahia, K.; Nabi, Z.; Tadjer, A.; Khalfi, A., Ab initio study of the structural and electronic properties of the complex structures of RuO₂. *Phys. B: Condens. Matter* **2003**, 339 (1), 1-10.
- 90. Yang, Z. J.; Li, J.; Linghu, R. F.; Cheng, X. L.; Yang, X. D., Optical and electronic properties of RuO₂ from first principles. *Can. J. Phys.* **2012**, *90* (5), 441-448.

- 91. Shiga, A.; Tsujiko, A.; Ide, T.; Yae, S.; Nakato, Y., Nature of Electrical Junction at the TiO₂/Substrate Interface for Particulate TiO₂ Film Electrodes in Aqueous Electrolytes. *J. Phys. Chem. B* **1998**, *102* (31), 6049-6055.
- 92. Nørskov, J. K.; Abild-Pedersen, F.; Studt, F.; Bligaard, T., Density functional theory in surface chemistry and catalysis. *PNAS* **2011**, *108* (3), 937.
- 93. Praserthdam, S.; Balbuena, P. B., Effects of oxygen coverage, catalyst size, and core composition on Pt-alloy coreshell nanoparticles for oxygen reduction reaction. *Catal. Sci. Tech.* **2016**, *6* (13), 5168-5177.
- 94. Jacobs, R.; Hwang, J.; Shao-Horn, Y.; Morgan, D., Assessing Correlations of Perovskite Catalytic Performance with Electronic Structure Descriptors. *Chem. Mater.* **2019**, *31* (3), 785-797.
- 95. Wang, L.; Huang, Z.; Du, Y.; Guo, S.; Jing, G., Rationalizing the promotional effect of Mn oxides in benzene combustion using an O 2p-band center descriptor. *Chem. Commun.* **2021**, *57* (40), 4942-4945.
- 96. Dronskowski, R.; Bloechl, P. E., Crystal orbital Hamilton populations (COHP): energy-resolved visualization of chemical bonding in solids based on density-functional calculations. *J. Phys. Chem.* **1993**, *97* (33), 8617-8624.
- 97. Deringer, V. L.; Tchougréeff, A. L.; Dronskowski, R., Crystal Orbital Hamilton Population (COHP) Analysis As Projected from Plane-Wave Basis Sets. *J. Phys. Chem. A* **2011**, *115* (21), 5461-5466.
- 98. Maintz, S.; Deringer, V. L.; Tchougréeff, A. L.; Dronskowski, R., Analytic projection from plane-wave and PAW wavefunctions and application to chemical-bonding analysis in solids. *J. Comput. Chem.* **2013**, *34* (29), 2557-2567.
- 99. Maintz, S.; Deringer, V. L.; Tchougréeff, A. L.; Dronskowski, R., LOBSTER: A tool to extract chemical bonding from plane-wave based DFT. *J. Comput. Chem.* **2016**, *37* (11), 1030-1035.
- 100. Godínez-Salomón, F.; Albiter, L.; Alia, S. M.; Pivovar, B. S.; Camacho-Forero, L. E.; Balbuena, P. B.; Mendoza-Cruz, R.; Arellano-Jimenez, M. J.; Rhodes, C. P., Self-Supported Hydrous Iridium–Nickel Oxide Two-Dimensional Nanoframes for High Activity Oxygen Evolution Electrocatalysts. *ACS Catal.* **2018**, *8* (11), 10498-10520.
- 101. Tang, W.; Sanville, E.; Henkelman, G., A grid-based Bader analysis algorithm without lattice bias. *J. Phys.: Condens. Matter* **2009**, *21* (8), 084204.
- 102. Sanville, E.; Kenny, S. D.; Smith, R.; Henkelman, G., Improved grid-based algorithm for Bader charge allocation. *J. Comput. Chem.* **2007**, *28* (5), 899-908.
- 103. Henkelman, G.; Arnaldsson, A.; Jónsson, H., A fast and robust algorithm for Bader decomposition of charge density. *Comput. Mater. Sci.* **2006**, *36* (3), 354-360.
- 104. Torun, E.; Fang, C. M.; de Wijs, G. A.; de Groot, R. A., Role of Magnetism in Catalysis: RuO₂ (110) Surface. *J. Phys. Chem. C* **2013**, *117* (12), 6353-6357.
- 105. Wang, C. S.; Freeman, A. J., Surface states, surface magnetization, and electron spin polarization: Fe(001). *Phys. Rev. B* **1981**, *24* (8), 4364-4371.
- 106. Choy, T.-S.; Chen, J.; Hershfield, S., Correlation between spin polarization and magnetic moment in ferromagnetic alloys. *J. Appl. Phys.* **1999**, *86* (1), 562-564.
- 107. Posysaev, S.; Miroshnichenko, O.; Alatalo, M.; Le, D.; Rahman, T. S., Oxidation states of binary oxides from data analytics of the electronic structure. *Comput. Mater. Sci.* **2019**, *161*, 403-414.

- 108. Crichton, R., Chapter 2 Basic Coordination Chemistry for Biologists. In *Biological Inorganic Chemistry (Third Edition)*, Crichton, R., Ed. Academic Press: 2019; pp 19-34
- 109. Duran, S.; Elmaalouf, M.; Odziomek, M.; Piquemal, J. Y.; Faustini, M.; Giraud, M.; Peron, J.; Tard, C., Electrochemical Active Surface Area Determination of Iridium-Based Mixed Oxides by Mercury Underpotential Deposition. *ChemElectroChem* **2021**, *8* (18), 3519-3524.
- 110. Dickens, C. F.; Montoya, J. H.; Kulkarni, A. R.; Bajdich, M.; Nørskov, J. K., An electronic structure descriptor for oxygen reactivity at metal and metal-oxide surfaces. *Surf. Sci.* **2019**, *681*, 122-129.
- 111. Nguyen-Phan, T. D.; Luo, S.; Vovchok, D.; Llorca, J.; Sallis, S.; Kattel, S.; Xu, W. Q.; Piper, L. F. J.; Polyansky, D. E.; Senanayake, S. D.; Stacchiola, D. J.; Rodriguez, J. A., Three-dimensional ruthenium-doped TiO₂ sea urchins for enhanced visible-light-responsive H-2 production. *Phys. Chem. Chem. Phys.* **2016**, *18* (23), 15972-15979.
- 112. Li, L. G.; Wang, P. T.; Shao, Q.; Huang, X. Q., Recent Progress in Advanced Electrocatalyst Design for Acidic Oxygen Evolution Reaction. *Adv. Mater.* **2021**, *33* (50).
- 113. Fang, Y. H.; Liu, Z. P., Mechanism and Tafel Lines of Electro-Oxidation of Water to Oxygen on RuO₂(110). *J. Am. Chem. Soc.* **2010**, *132* (51), 18214-18222.
- 114. Camacho-Forero, L. E.; Godínez-Salomón, F.; Ramos-Sánchez, G.; Rhodes, C. P.; Balbuena, P. B., Theoretical and Experimental Study of the Effects of Cobalt and Nickel Doping within IrO₂ on the Acidic Oxygen Evolution Reaction. *J. Catal.* **2022**, *408*, 64-80.
- 115. Valdés, Á.; Qu, Z. W.; Kroes, G. J.; Rossmeisl, J.; Nørskov, J. K., Oxidation and Photo-Oxidation of Water on TiO₂ Surface. *J. Phys. Chem. C* **2008**, *112* (26), 9872-9879.
- 116. Dixit, M.; Markovsky, B.; Schipper, F.; Aurbach, D.; Major, D. T., Origin of Structural Degradation During Cycling and Low Thermal Stability of Ni-Rich Layered Transition Metal-Based Electrode Materials. *J. Phys. Chem. C* **2017**, *121* (41), 22628-22636.
- 117. Roling, L. T.; Abild-Pedersen, F., Structure-Sensitive Scaling Relations: Adsorption Energies from Surface Site Stability. *ChemCatChem* **2018**, *10* (7), 1643-1650.
- 118. Rossmeisl, J.; Qu, Z. W.; Zhu, H.; Kroes, G. J.; Norskov, J. K., Electrolysis of water on oxide surfaces. *J. Electroanal. Chem.* **2007**, *607* (1-2), 83-89.
- 119. Kibsgaard, J.; Chorkendorff, I., Considerations for the scaling-up of water splitting catalysts. *Nat. Energy* **2019**, *4* (6), 430-433
- 120. Reier, T.; Pawolek, Z.; Cherevko, S.; Bruns, M.; Jones, T.; Teschner, D.; Selve, S.; Bergmann, A.; Nong, H. N.; Schlogl, R.; Mayrhofer, K. J. J.; Strasser, P., Molecular Insight in Structure and Activity of Highly Efficient, Low-Ir Ir-Ni Oxide Catalysts for Electrochemical Water Splitting (OER). *J. Am. Chem. Soc.* **2015**, *137* (40), 13031-13040.
- 121. Burnett, D. L.; Petrucco, E.; Rigg, K. M.; Zalitis, C. M.; Lok, J. G.; Kashtiban, R. J.; Lees, M. R.; Sharman, J. D. B.; Walton, R. I., (M,Ru)O₂(M = Mg, Zn, Cu, Ni, Co) Rutiles and Their Use as Oxygen Evolution Electrocatalysts in Membrane Electrode Assemblies under Acidic Conditions. *Chem. Mat.* **2020**, *32* (14), 6150-6160.
- 122. Geiger, S.; Kasian, O.; Ledendecker, M.; Pizzutilo, E.; Mingers, A. M.; Fu, W. T.; Diaz-Morales, O.; Li, Z. Z.; Oellers, T.; Fruchter, L.; Ludwig, A.; Mayrhofer, K. J. J.; Koper, M. T. M.; Cherevko, S., The stability number as a metric

- for electrocatalyst stability benchmarking. *Nat. Catal.* **2018,** *I* (7), 508-515.
- 123. Manoharan, R.; Goodenough, J. B., Electrochemical Behavior of RuTi. *Electrochim. Acta* **1991**, *36* (1), 19-26.
- 124. Kim, Y. T.; Lopes, P. P.; Park, S. A.; Lee, A. Y.; Lim, J.; Lee, H.; Back, S.; Jung, Y.; Danilovic, N.; Stamenkovic, V.; Erlebacher, J.; Snyder, J.; Markovic, N. M., Balancing activity, stability and conductivity of nanoporous core-shell iridium/iridium oxide oxygen evolution catalysts. *Nat. Commun.* **2017**, *8*, 8.
- 125. Kasian, O.; Grote, J. P.; Geiger, S.; Cherevko, S.; Mayrhofer, K. J. J., The Common Intermediates of Oxygen Evolution and Dissolution Reactions during Water Electrolysis on Iridium. *Angew. Chem. Int. Ed.* **2018**, *57* (9), 2488-2491.
- 126. Binninger, T.; Mohamed, R.; Waltar, K.; Fabbri, E.; Levecque, P.; Kotz, R.; Schmidt, T. J., Thermodynamic explanation of the universal correlation between oxygen evolution activity and corrosion of oxide catalysts. *Sci Rep* **2015**, *5*, 7.
- 127. Hodnik, N.; Jovanovic, P.; Pavlisic, A.; Jozinovic, B.; Zorko, M.; Bele, M.; Selih, V. S.; Sala, M.; Hocevar, S.; Gaberscek, M., New Insights into Corrosion of Ruthenium and Ruthenium Oxide Nanoparticles in Acidic Media. *J. Phys. Chem. C* **2015**, *119* (18), 10140-10147.
- 128. Ryckaert, J.-P.; Ciccotti, G.; Berendsen, H. J. C., Numerical integration of the cartesian equations of motion of a

- system with constraints: molecular dynamics of n-alkanes. *J. Comput. Phys.* **1977**, *23* (3), 327-341.
- 129. Carter, E. A.; Ciccotti, G.; Hynes, J. T.; Kapral, R., Constrained reaction coordinate dynamics for the simulation of rare events. *Chem. Phys. Lett.* **1989**, *156* (5), 472-477.
- 130. Den Otter, W. K.; Briels, W. J., Free energy from molecular dynamics with multiple constraints. *Mol. Phys.* **2000**, *98* (12), 773-781.
- 131. Darve, E.; Wilson, M. A.; Pohorille, A., Calculating Free Energies Using a Scaled-Force Molecular Dynamics Algorithm. *Mol. Simul.* **2002**, *28* (1-2), 113-144.
- 132. Fleurat-Lessard, P.; Ziegler, T., Tracing the minimum-energy path on the free-energy surface. *J. Chem. Phys.* **2005**, *123* (8), 084101.
- 133. Ciccotti, G.; Ferrario, M., Blue Moon Approach to Rare Events. *Mol. Simul.* **2004**, *30* (11-12), 787-793.
- 134. Komeiji, Y., Implementation of the blue moon ensemble method. *Chem-Bio Info. J.* **2007**, *7* (1), 12-23.
- 135. Bucko, T., *Ab initio* calculations of free-energy reaction barriers. *J. Phys.: Condens. Matter* **2008**, *20* (6), 064211.

Table of Contents artwork

